

## EUROPIUM, SAMARIUM, AND NEODYMIUM ISOTOPIC FRACTIONS IN METAL-POOR STARS

IAN U. ROEDERER<sup>1</sup>, JAMES E. LAWLER<sup>2</sup>, CHRISTOPHER SNEDEN<sup>1</sup>, JOHN J. COWAN<sup>3</sup>, JENNIFER S. SOBECK<sup>1,4</sup>, CATHERINE A. PILACHOWSKI<sup>5</sup>

*Draft version October 31, 2018*

### ABSTRACT

We have derived isotopic fractions of europium, samarium, and neodymium in two metal-poor giants with differing neutron-capture nucleosynthetic histories. These isotopic fractions were measured from new high resolution ( $R \sim 120,000$ ), high signal-to-noise ( $S/N \sim 160\text{--}1000$ ) spectra obtained with the 2dCoudé spectrograph of McDonald Observatory’s 2.7 m Smith telescope. Synthetic spectra were generated using recent high-precision laboratory measurements of hyperfine and isotopic subcomponents of several transitions of these elements and matched quantitatively to the observed spectra. We interpret our isotopic fractions by the nucleosynthesis predictions of the stellar model, which reproduces  $s$ -process nucleosynthesis from the physical conditions expected in low-mass, thermally-pulsing stars on the AGB, and the classical method, which approximates  $s$ -process nucleosynthesis by a steady neutron flux impinging upon Fe-peak seed nuclei. Our Eu isotopic fraction in HD 175305 is consistent with an  $r$ -process origin by the classical method and is consistent with either an  $r$ - or an  $s$ -process origin by the stellar model. Our Sm isotopic fraction in HD 175305 suggests a predominantly  $r$ -process origin, and our Sm isotopic fraction in HD 196944 is consistent with an  $s$ -process origin. The Nd isotopic fractions, while consistent with either  $r$ -process or  $s$ -process origins, have very little ability to distinguish between *any* physical values for the isotopic fraction in either star. This study for the first time extends the  $n$ -capture origin of multiple rare earths in metal-poor stars from elemental abundances to the isotopic level, strengthening the  $r$ -process interpretation for HD 175305 and the  $s$ -process interpretation for HD 196944.

*Subject headings:* atomic data — nuclear reactions, nucleosynthesis, abundances — stars: abundances — stars: Population II

### 1. INTRODUCTION

A wealth of observational studies over the last decade have focused on measuring precise abundances of neutron ( $n$ )-capture elements in metal-poor stars. The heart of this enterprise is identifying the origin of the nuclides with  $Z > 30$  in our Galaxy. These nuclides are produced in stars through either the rapid ( $r$ )-process or the slow ( $s$ )-process. Rapid-process nucleosynthesis occurs in environments with high neutron fluxes and densities, allowing many neutrons to be captured by existing nuclei much more rapidly than the timescales for  $\beta$ -decay. Slow-process nucleosynthesis occurs where the neutron densities are lower, with  $\beta$ -decay timescales generally shorter than the times between  $n$ -capture events. To build heavy nuclei through the  $s$ -process, a chain of stable or long-lived nuclei must exist from the existing seed nucleus to the final product. The  $r$ -process and  $s$ -process lead to the creation of different sets of heavy nuclei, some of which can only be created in one process or the other (“pure-

$s$ -” or “pure- $r$ -nuclei”) and some of which are created by both processes (see, e.g., Cowan & Sneden 2006). While the precise astrophysical site(s) of the  $r$ -process have yet to be identified,  $s$ -process nucleosynthesis takes place in low- and intermediate-mass stars on the asymptotic giant branch (AGB) (e.g., Busso et al. 1999).

To illustrate the effects of both  $n$ -capture processes, in Figure 1 we show a table of nuclides covering portions of the atomic number domain  $60 \leq Z \leq 63$ . The  $s$ -process can add only one neutron before a  $\beta$ -decay occurs for an unstable nucleus. On the other hand, the  $r$ -process quickly floods a target nucleus with many neutrons, overwhelming the  $\beta$ -decay rates. When neutrons are no longer being added, the nucleus will  $\beta$ -decay repeatedly until it reaches stability. For isotopes produced primarily in the  $s$ -process (e.g.,  $^{146}\text{Nd}$ ,  $^{148,150}\text{Sm}$ ) a stable isotope with one less nuclide always exists. For isotopes produced primarily or wholly by the  $r$ -process (e.g.,  $^{150}\text{Nd}$ ,  $^{147,149,152,154}\text{Sm}$ ), there is a clear path for  $\beta$ -decay from unstable nuclei to the lower right (in the table of nuclides) of the stable  $r$ -process isotope, sometimes unreachable by the  $s$ -process.

The nucleosynthetic signatures of the  $s$ - and  $r$ -processes stand in sharp contrast to one-another. The Solar System (S. S.) isotopic abundances are well-established from studies of CI meteorites, as summarized in, e.g., Anders & Grevesse (1989) and Lodders (2003). Two primary methods are used to decompose the S. S. isotopic abundances into their constituent  $s$ - and  $r$ -process origins. In the “standard” or “classical” method, first articulated by Clayton et al. (1961) and

<sup>1</sup> Department of Astronomy, University of Texas at Austin, 1 University Station, C1400, Austin, TX 78712-0259; iur.chris@astro.as.utexas.edu

<sup>2</sup> Department of Physics, University of Wisconsin, 1150 University Avenue, Madison, WI 53706; jelawler@wisc.edu

<sup>3</sup> Department of Physics and Astronomy, University of Oklahoma, Room 131, Nielsen Hall, Norman, OK 73019; cowan@nhn.ou.edu

<sup>4</sup> European Southern Observatory, Karl-Schwarzschild-Strasse 2, D-85748 Garching bei München, Germany; jsoback@eso.org

<sup>5</sup> Department of Astronomy, Indiana University, Swain West 319, 727 East Third Street, Bloomington, IN 47405-7105; catyp@astro.indiana.edu

Seeger et al. (1965) and with abundances later updated by, e.g., Käppeler et al. (1989); Burris et al. (2000); Simmerer et al. (2004), and Cowan et al. (2006), the  $s$ -process is modeled as a slowly-varying function of neutron exposure. This method attempts to smoothly fit the “ $\sigma N_s$ ” curve (the product of the  $n$ -capture cross-section and the S. S.  $s$ -process abundances) using lab measurements of  $\sigma$  to determine  $N_s$ . In the “stellar” model of Arlandini et al. (1999), isotopic abundances for  $s$ -process nucleosynthesis in  $1.5\text{--}3.0 M_\odot$  stars are predicted based upon nuclear physics cross sections and stellar model calculations for thermally-pulsing (TP) stars on the AGB. In both of these cases, the  $r$ -process abundances are then derived as residuals between the total S. S. abundances and the  $s$ -process products. Both approaches have strengths and weaknesses. The classical method is model-independent, but it assumes an empirical, smoothly-varying relationship for the  $\sigma N_s$  abundance curve (which relies on the measured S. S. abundances) and ignores details of the nuclear physics. The stellar model does not depend on knowledge of the S. S. abundance distribution, but is heavily dependent on nuclear physics laboratory measurements and complex stellar AGB model calculations.

These models can also be used to predict the relative amounts of  $s$ - or  $r$ -process nucleosynthesis products in metal-poor stars. Several key rare earth elements are commonly used to assess  $r$ -/ $s$ -process abundance dominance in stars.<sup>6</sup> Eu is commonly used as a surrogate for  $r$ -process nucleosynthesis because it is so predominantly composed of  $r$ -process material and has several easily-observed spectral lines. Similarly, Ba or La are commonly used as surrogates of  $s$ -process nucleosynthesis. Thus, many studies have employed [Ba/Eu]<sup>7</sup> ratios in metal-poor stars to estimate the relative contributions from the  $s$ - and  $r$ -processes (e.g., Spite & Spite 1978; Gratton & Sneden 1994; Burris et al. 2000; Mashonkina et al. 2003; Honda et al. 2004b; Barklem et al. 2005; François et al. 2007), which in turn constrain models of chemical evolution in the early Galaxy (Travaglio et al. 1999, 2001; Cescutti et al. 2006; Kratz et al. 2007). Recently, [La/Eu] ratios have been employed as an alternative to [Ba/Eu] to avoid difficulties in Ba abundance determinations (see, e.g., Simmerer et al. 2004; Jonsell et al. 2006; Winckler et al. 2006).

Elemental abundances, the sums of abundances of their naturally-occurring constituent isotopes, are more easily measured in stars than the isotopic abundances; however, isotopic abundances should be more fundamental indicators of  $n$ -capture nucleosynthesis because they can directly confront  $r$ -process and  $s$ -process predictions without the smearing effect of multiple isotopes. Much recent evidence (e.g., the growing number of  $r$ -process-enhanced stars that conform to the scaled-S. S.  $r$ -process elemen-

tal abundance distribution) supports the hypothesis of a universal  $r$ -process mechanism for elements with  $Z \geq 56$ . It is important to demonstrate that the  $r$ -process elemental abundance pattern extends to the isotopic level. Such agreement would greatly strengthen the argument for a universal  $r$ -process mechanism for the heavy  $n$ -capture elements.

Most isotope fractions, unlike elemental abundances, are very insensitive to the model atmosphere parameters. The wavelength of a spectral line is split by two effects, hyperfine structure (HFS) and isotope shifts, and the isotopic fractions can be measured by detailed comparisons of an observed absorption line profile to synthetic spectra of these line substructures. If this splitting is comparable to or greater than the combined effects of stellar thermal, macroturbulent, and rotational broadening and the broadening caused by the spectrograph slit, then it may be possible to measure the isotopic fractions. In principle, unlike with elemental abundances, any  $n$ -capture element with multiple naturally-occurring isotopes that are produced in different amounts by the  $s$ - and  $r$ -processes can be used to assess the relative  $s$ - and  $r$ -process contributions to the stellar composition. In practice, the availability of quality atomic data has limited studies of isotopic fractions of rare earth elements in stars, but the relatively recent increase in laboratory spectral line substructure studies has led to the identification of a few lines of a few elements that might be analyzed at the isotopic level.

Cowley & Frey (1989) and Magain & Zhao (1993a) first suggested that the width of the Ba II 4554Å line in stellar spectra would be sensitive to the isotopic fraction. Magain & Zhao (1993a), Magain (1995), and Lambert & Allende Prieto (2002) all examined the Ba isotopic fraction in the metal-poor subgiant HD 140283. Their measured isotopic fractions had uncertainties too large to unambiguously discern the Ba nucleosynthetic origin in this star. A recent series of papers by Mashonkina et al. (1999, 2003) and Mashonkina & Zhao (2006) have measured Ba isotopic fractions in thin and thick disk stars. Their approach is to set the Ba elemental abundance from lines not affected by HFS or isotope shifts and then to derive the isotopic fraction from the 4554Å line, whose shape is sensitive to both its elemental abundance and isotopic composition of Ba. Mashonkina & Zhao (2006) clearly show that a higher fraction of  $r$ -process Ba isotopes is present in thick disk stars than in S. S. material and thin disk stars, and they also show that a smooth trend of increasing  $s$ -process contributions occurs with increasing metallicity. Since only the 4554Å line is useful for examining the Ba isotopic mix, and the profile of this line is known to suffer from non-LTE effects in metal-poor stars (e.g., Mashonkina et al. 1999; Short & Hauschildt 2006), we do not attempt to assess the Ba isotopic fractions in this study. The Mashonkina et al. studies of the Ba isotopic fraction do, however, employ non-LTE calculations.

Eu isotopic fractions in metal-poor stars were first reported by Sneden et al. (2002), who found that the isotopic ratio in three  $r$ -process-rich giants was consistent with the S. S. isotopic ratio. Subsequent studies by Aoki et al. (2003a,b) found that Eu isotopic ratios could marginally distinguish  $s$ - and  $r$ -process contributions in

<sup>6</sup> The  $s$ -process percentages for some of the commonly-studied rare earth elements, predicted by the stellar model and classical method, respectively, are: Ba (five naturally-occurring isotopes), 81.1% or 85.3%; La (one isotope), 62.1% or 75.4%; Nd (seven isotopes), 58.8% or 57.9%; Sm (seven isotopes), 30.7% or 33.1%; Eu (two isotopes), 5.8% or 2.3%.

<sup>7</sup> We adopt the usual spectroscopic notations that  $[A/B] \equiv \log_{10}(N_A/N_B)_* - \log_{10}(N_A/N_B)_\odot$ , and that  $\log \varepsilon(A) \equiv \log_{10}(N_A/N_H) + 12.00$ , for elements A and B.

stars that had previously been shown to exhibit such chemical signatures. Lundqvist et al. (2007) have investigated the Sm isotopic fractions in a very metal-poor  $r$ -process-enriched star, qualitatively showing that the isotopic mix is in agreement with an  $r$ -process origin. No measurements of the Nd isotopic fraction have been made outside of the S. S., and no study has yet attempted to measure isotopic fractions of multiple  $n$ -capture elements in the same star.

In our study, we analyze the isotopic fractions of Eu, Sm, and Nd in two metal-poor giant stars. Our observations and methods of analysis are described in § 2 and 4, respectively. We summarize the available atomic data for each species in § 3. Our measurements of the elemental abundances and isotopic fractions are presented in § 5 and § 6. In § 7 we discuss the implications of our measurements in the context of using isotopic fractions of multiple species to constrain the  $s$ - and  $r$ -process nucleosynthetic histories. In § 8 we use Eu and Pb abundances collected from the literature to assess the  $s$ -process model predictions for the  $^{151}\text{Eu}$  isotope, since pure- $r$ - and pure- $s$ -process nucleosynthesis reactions produce such contrasting abundances of these elements. We also make suggestions for how future studies might utilize measurements of  $n$ -capture isotopic fractions to make similar comparisons for other isotopes in § 9. We summarize our results in § 10. In the appendices, we include comments describing the nuances associated with analyzing each line of each species (Appendix A), and we include our computations of the hyperfine structure subcomponents for both Sm (Appendix B) and Nd (Appendix C).

## 2. OBSERVATIONS

### 2.1. Selection of Target Stars

We choose two bright, metal-poor giants for our analysis, HD 175305 and HD 196944. The technical requirements of achieving high signal-to-noise (S/N) ratios at very high resolution on a telescope with a moderate aperture mandate that we select bright ( $V \lesssim 8.5$ ) targets. We select metal-poor giant stars for this analysis because (1) metal-poor stars present significantly less crowding of strong absorption features in the blue spectral region where the lines of interest are concentrated, (2) absorption lines of all species will exhibit greater line depth in giants than in dwarfs because of the decrease in the continuous opacity with decreasing electron pressure in giants, and (3) at a given metallicity, molecular formation will be less in giants than in dwarfs. To maximize the expected contrast in the isotopic fractions, we have deliberately selected stars with different chemical enrichment histories. Although these stars have been well-studied, no previous attempts have been made to examine their isotopic fractions.

HD 175305 is a metal-poor ( $[\text{Fe}/\text{H}] = -1.6$ ), bright ( $V \sim 7.2$ ) giant that was selected because it shows evidence of  $r$ -process enrichment ( $[\text{Eu}/\text{Fe}] \sim +0.5$ ,  $[\text{Ba}/\text{Eu}] < 0.0$ ,  $[\text{La}/\text{Eu}] \sim -0.4$ ; Burris et al. 2000; Fulbright 2000; Cowan et al. 2005). HD 175305 is not enriched in carbon ( $[\text{C}/\text{Fe}] = +0.2$ ; Wallerstein et al. 1979). Although only a handful of heavy  $n$ -capture abundances have been measured previously, the high  $[\text{Eu}/\text{Fe}]$  and low  $[\text{Ba}/\text{Eu}]$  ratios are suggestive of an

$r$ -process origin. Combining Cowan et al. (2005)'s abundance measurements of osmium (Os,  $Z = 76$ ), iridium (Ir,  $Z = 77$ ), and platinum (Pt,  $Z = 78$ ) from UV spectra and Lawler et al. (2007)'s measurement of hafnium (Hf,  $Z = 72$ ) with additional heavy  $n$ -capture elemental abundances measured in our spectra will produce a more thorough understanding of this star's enrichment history to complement our isotopic fraction measurements.

HD 196944 is a very metal-poor ( $[\text{Fe}/\text{H}] = -2.4$ ), bright ( $V \sim 8.4$ ) giant with clear  $s$ -process signatures. This star has high C, N, and O abundances ( $[\text{C}/\text{Fe}] \sim +1.3$ ,  $[\text{N}/\text{Fe}] \sim +1.3$ ,  $[\text{O}/\text{Fe}] \sim +1.4$ ; Zács et al. 1998; Aoki et al. 2002; Jonsell et al. 2005), high Ba and La abundances ( $[\text{Ba}/\text{Fe}] \sim +1.1$ ,  $[\text{La}/\text{Fe}] \sim +0.9$ ), a low Eu abundance ( $[\text{Eu}/\text{Fe}] \sim +0.2$ ), and a large overabundance of lead ( $[\text{Pb}/\text{Fe}] \sim +2.0$ ; Van Eck et al. 2001; Aoki et al. 2002; Van Eck et al. 2003). HD 196944 also exhibits radial velocity variations (Lucatello et al. 2005), indicating that it is a member of a binary or multiple star system. These characteristics have led to the classification of HD 196944 as a carbon-enhanced metal-poor  $s$ -enriched (CEMP- $s$ ) star, as defined in Beers & Christlieb (2005). Gallino et al. (2005) have shown that the abundance pattern of HD 196944 can be reproduced by assuming mass transfer of material enriched in  $s$ -process elements from a companion star with an initial mass of  $1.5 M_{\odot}$  that passed through the TP-AGB phase.

We also observed HD 122563 in our study; at  $V \sim 6.2$ , this star is the brightest very metal-poor ( $[\text{Fe}/\text{H}] = -2.8$ ) star in the sky. Unfortunately the lines of Eu, Sm, and Nd proved to be too weak to provide any assessment of the isotopic fractions. This is unfortunate because Honda et al. (2007), following studies of this star by Cowan et al. (2005), Aoki et al. (2005), and Honda et al. (2006), have suggested that HD 122563 and HD 88609 may be the first two known representatives of a class of stars whose  $n$ -capture enrichment has been dominated by the weak  $r$ -process, which produces a distinctly different abundance pattern than the main  $r$ -process.<sup>8</sup> Our analysis of HD 122563 did allow us to assess the location and strength of blending features for some of our lines of interest. It is possible that the Eu II lines at 3819, 3907, and 4129Å, which were not covered in our spectrum, may give some hint to the Eu isotopic fraction.

### 2.2. Description of Observations

For a set of lines of a given species with the same ionization state in a stellar atmosphere, the relative strength of each line depends on its transition probability, excitation potential, wavelength, and the continuous opacity of the atmosphere at that wavelength (see, e.g., Gray 2005, p. 389). In metal-poor stars the continuous opacity (from  $\text{H}^-$ ) increases slowly over the visible wavelength region as the wavelength increases; these two terms take opposite signs in calculations of the line strength and roughly offset each other. To first approximation then, the relative strengths of individual absorption lines are determined by the transition properties of the lines themselves. Figure 10 of Lawler et al. (2006) illustrates this point for the

<sup>8</sup> Please see, e.g., Wasserburg et al. 1996, Qian & Wasserburg 2000, Wasserburg & Qian 2000, Johnson & Bolte 2002, Wanajo & Ishimaru 2006, and Kratz et al. 2007 for further discussion of these two processes.

case of Sm II lines. For the  $n$ -capture species considered in our study, the first-ionized state is dominant in our stars, and most of the transitions have similar excitation potentials ( $\sim 0.0$ – $0.7$  eV), so the oscillator strengths most significantly affect the relative line strength. The  $\log(gf)$  values generally decrease when moving from the near-UV to the near-IR spectral regions, so the strongest lines in stellar spectra tend to lie in the near-UV and blue end of the visible spectrum. This is unfortunately where the most severe blending with other spectral features is likely to occur. The isotope shifts increase with increasing wavelength; this broadens the stellar line profiles, making it easier to measure the isotopic fraction. The decrease in line strength, decrease in blending features, and the increase in isotopic shifts at longer wavelengths compete against each other, producing a range in the visible spectrum from  $\sim 4400$ – $5100\text{\AA}$  where isotopic fractions are most easily measured.

We acquired new observations of our target stars using the 2dCoudé cross-dispersed echelle spectrograph (Tull et al. 1995) on the 2.7 m Harlan J. Smith Telescope at the W. J. McDonald Observatory. Observations of HD 122563 and HD 196944 were made on 2006 June 12–18, and observations of HD 175305 were made on 2006 August 08–12. Sets of 30-minute exposures were taken with a Tektronix 2048  $\times$  2048 CCD (“TK3”). Around  $5000\text{\AA}$ , to sample the full width of a line profile ( $\sim 0.2\text{\AA}$ ) with at least 10 points requires  $\Delta\lambda \approx 0.02$  per pixel and a two-pixel resolution of  $R \sim 125,000$ . This requirement dictates the spectral resolution necessary to complete our analysis. Our data have FWHM resolving powers  $R \sim 120,000$ . Lines in our Th–Ar comparison spectra can be fit with a pure Gaussian function, and no variation in the instrumental profile was found from night-to-night over the course of either observing run. Due to the limited wavelength coverage at this setup, we have observed each star with three grating settings to increase the wavelength coverage. Our spectra cover  $4200 \leq \lambda \leq 6640\text{\AA}$  in HD 122563 and HD 196944 and  $4120 \leq \lambda \leq 5890\text{\AA}$  in HD 175305; however, even when using multiple grating settings our wavelength coverage is still incomplete within these ranges.

Image processing, order extraction, and wavelength calibration were performed using standard IRAF<sup>9</sup> tasks in the *echelle* and *onedspec* packages. Echelle orders were cross-correlated and co-added, and the continuum normalization was performed with the SPECTRE software package (Fitzpatrick & Sneden 1987). Our final S/N values (per pixel) range from  $\sim 160$  at  $4130\text{\AA}$  to  $\sim 330$  at  $5100\text{\AA}$  in HD 175305,  $\sim 160$  at  $4200\text{\AA}$  to  $\sim 400$  at  $5000\text{\AA}$  in HD 196944, and  $\sim 430$  at  $4200\text{\AA}$  to  $\sim 1000$  at  $5000\text{\AA}$  in HD 122563.

### 3. ATOMIC DATA

#### 3.1. HFS Structure and Isotope Shifts

HFS is primarily caused by the magnetic interaction between an electron and the nucleus of an atom. This interaction occurs when the nucleus has a magnetic dipole

moment that results from a non-zero angular momentum, which occurs when the nucleus has an odd number of protons and/or an odd number of neutrons. The strength of this interaction is characterized by the magnetic dipole “A” constant, which can be measured in laboratory studies. We also include the measured electric quadrupole interaction “B” constant in our HFS computations, but magnetic interaction is usually dominant. In stellar spectra, HFS is manifest as a broadening of a single line of a particular atom due to the energy shifts. Isotope shifts, on the other hand, are slight rearrangements of the energy levels of one isotope of a particular species relative to another isotope of the same species. The most useful lines of heavy atoms—such as those considered in this study—usually have isotope shifts dominated by the field shift. This shift is from the finite volume occupied by the nucleus of an atom. Proton charge is distributed within the nucleus, and not concentrated at the origin, hence the electric field inside the nucleus does not have a  $1/r$  dependence. For electrons that have a significant probability of existing at small  $r$ , such as the  $6s$  electron in the ground state configuration of Eu II, this can have a sizable effect. Both the reduced mass shifts and specific mass shifts of the upper and lower levels also contribute to the total isotope shifts of a line. Isotope shifts for our elements have been measured in laboratory experiments. In stellar spectra, the effect of isotope shifts is to broaden the absorption line profile when more than one isotope of the same atom are present in the stellar atmosphere.

#### 3.2. Europium Atomic Data

There are two naturally-occurring isotopes of Eu:  $^{151}\text{Eu}$  (47.8% S. S.) and  $^{153}\text{Eu}$  (52.2%). Both Eu isotopes exhibit HFS. Both isotopes of Eu are produced in roughly equal amounts in the  $r$ -process, which dominates over the  $s$ -process as the origin of the S. S. Eu. Because there are only two Eu isotopes, it is straightforward to measure the isotopic fraction by measuring the fraction of one of these isotopes relative to the total amount of Eu. The fraction  $f_{151}$  is defined as

$$f_{151} = \frac{N(^{151}\text{Eu})}{N(\text{Eu})}. \quad (1)$$

In Table 2, we list the fraction of  $^{151}\text{Eu}$  that would be expected if all the Eu present in a given star were to have originated in only the  $s$ -process or the  $r$ -process for both the stellar model and classical method. The stellar model predicts a  $f_{151}^s$  abundance that is consistent with two ( $r+s$ )-enriched stars (Aoki et al. 2003b, 2006), but the classical method predicts a  $f_{151}^s$  abundance that is nearly 30 times smaller. We also note that even the predictions for the pure- $s$ -process abundance of  $^{151}\text{Eu}$  vary greatly within different sets of classical method calculations (Arlandini et al. 1999; Cowan et al. 2006), so this discrepancy is not limited to only the classical method versus stellar model predictions. Lengthy discussion of this discrepancy will be taken up further in § 8.

We adopt the Eu II  $\log(gf)$  values of Lawler et al. (2001b). The hyperfine and isotopic components are taken from Ivans et al. (2006). The HFS of the three Eu II lines that we consider is very wide,  $\sim 0.2$ – $0.3\text{\AA}$ , which facilitates our ability to measure the isotopic fraction.

<sup>9</sup> IRAF is distributed by the National Optical Astronomy Observatories, which are operated by the Association of Universities for Research in Astronomy, Inc., under cooperative agreement with the National Science Foundation.

### 3.3. Samarium Atomic Data

There are seven naturally-occurring isotopes of Sm:  $^{144}\text{Sm}$  (3.1% S. S.),  $^{147}\text{Sm}$  (15.0%),  $^{148}\text{Sm}$  (11.2%),  $^{149}\text{Sm}$  (13.8%),  $^{150}\text{Sm}$  (7.4%),  $^{152}\text{Sm}$  (26.7%), and  $^{154}\text{Sm}$  (22.8%). The  $^{144}\text{Sm}$  isotope is exclusively produced by the  $p$ -process; fortunately for this analysis, this isotope only comprises 3.1% of the Sm in the S. S., so we can neglect its contribution to the isotopic mix. According to the stellar model and classical method,  $^{148}\text{Sm}$  and  $^{150}\text{Sm}$  are produced exclusively by the  $s$ -process, while the  $r$ -process dominates the production of the other four isotopes.

The two odd- $A$  isotopes exhibit HFS structure in addition to the energy shifts between all seven isotopes. The Sm isotope shifts are  $\sim 0.05 - 0.10 \text{ \AA}$ , which is slightly larger than the Sm HFS splittings,  $\sim 0.05 \text{ \AA}$ , yet both the Sm isotope shifts and HFS splittings are significantly smaller than the Eu HFS splittings. The two heaviest isotopes,  $^{152}\text{Sm}$ , and  $^{154}\text{Sm}$ , have large isotope shifts relative to the isotope shifts of the lighter five isotopes in many of the transitions we analyze here (cf. Figures 1 and 2 of Lundqvist et al. 2007). Therefore, it makes sense to define the isotopic fraction in terms of these two heaviest isotopes. The quantity  $f_{152+154}$  is defined by

$$f_{152+154} = \frac{N(^{152}\text{Sm}) + N(^{154}\text{Sm})}{N(\text{Sm})}. \quad (2)$$

In Table 2, we also list the isotopic fraction of Sm that would be expected if all the Sm present in a particular star were to have originated in only the  $s$ -process or the  $r$ -process for both the stellar model and classical method. Note that this definition more easily distinguishes pure- $s$  and pure- $r$  isotopes of Sm than the  $f_{\text{odd}}$  definition suggested in § 7 of Lawler et al. (2006). In addition, the pure- $s$  and pure- $r$  isotope fractions predicted by the stellar model and classical method do not differ significantly when expressed in terms of  $f_{152+154}$ .

We have computed the HFS structure patterns for 13 Sm lines in this wavelength range using the hyperfine A and B constants and isotope shifts of Masterman et al. (2003), when available, supplemented with additional values from Lundqvist et al. (2007) and others as described in Appendix B. Three of these lines (4719, 5052, and 5103) do not have complete sets of hyperfine A and B constants reported in the literature. To gauge the impact of the HFS splitting on our stellar syntheses, we have compared two syntheses of lines with full sets of hyperfine A and B constants, one including the HFS splitting and isotope shifts and one including only the isotope shifts. Syntheses with a lower fraction of  $f_{152+154}$  are slightly more broadened in the case of full HFS treatment than when only the isotope shifts are considered. The differences are small; the synthesis including HFS is  $\approx 5-6\%$  wider at FWHM than the synthesis with no HFS (when the percentage of isotopes exhibiting HFS is maximized in the synthesis). Nevertheless we recommend that lines lacking complete sets of hyperfine A and B constants should not be used to measure the isotopic fraction by fitting the shape of the line profile; however, they should still be useful for other methods of measuring the isotopic fraction and for elemental abundance analyses and are included in the discussion here for this reason. We

adopt the Sm II  $\log(gf)$  values of Lawler et al. (2006).

### 3.4. Neodymium Atomic Data

Nd, like Sm, has seven naturally-occurring isotopes in S. S. material:  $^{142}\text{Nd}$  (27.2% S. S.),  $^{143}\text{Nd}$  (12.2%),  $^{144}\text{Nd}$  (23.8%),  $^{145}\text{Nd}$  (8.3%),  $^{146}\text{Nd}$  (17.2%),  $^{148}\text{Nd}$  (5.7%), and  $^{150}\text{Nd}$  (5.6%). The lightest isotope is only produced in the  $s$ -process, the two heaviest isotopes are almost exclusively produced in the  $r$ -process, and the other four isotopes are produced in a combination of the two processes. The two odd- $A$  isotopes exhibit HFS structure, like Sm. Rosner et al. (2005) have measured the isotope shifts and HFS A and B constants for Nd transitions between 4175 and 4650  $\text{\AA}$ . For the lines examined in our study, the Nd II HFS is comparable in scale to the Sm II HFS,  $\lesssim 0.05 \text{ \AA}$ , while the Nd II isotope shifts are relatively small, usually only  $\lesssim 0.025 \text{ \AA}$ . Den Hartog et al. (2003) measured  $\log(gf)$  values for many of these transitions and noted that several of the yellow-red lines (mostly redward of 5100  $\text{\AA}$ ) exhibited a doublet or triplet structure in their FTS profiles.

We collect the Nd isotopes into fractions that might provide a good indication of pure- $s$ - and pure- $r$ -nucleosynthesis while making sensible choices about which sets of isotopes are shifted the most from one another. We adopt the Nd isotopic fraction defined by

$$f_{142+144} = \frac{N(^{142}\text{Nd}) + N(^{144}\text{Nd})}{N(\text{Nd})}. \quad (3)$$

Predictions for this isotopic fraction are displayed in Table 2. Note that the pure- $s$  and pure- $r$  predictions of the stellar model and classical method generally agree well for  $f_{142+144}$ . In Appendix C we present our calculations of the HFS structure patterns for 6 Nd lines in the wavelength region covered by our spectra.

## 4. ANALYSIS

### 4.1. Radial Velocities

To measure the radial velocities, we find the centroid of  $\sim 17-19$  Fe I lines and calibrate to the wavelengths in Learner & Thorne (1988)<sup>10</sup>, which are accurate to better than  $0.3 \text{ m\AA}$ . We find our wavelength scale zeropoint from a small number of telluric lines in the reddest orders of our spectra. Heliocentric velocities for each observation are calculated using the IRAF *rvcorrect* task. For HD 175305 and HD 122563, we measure heliocentric radial velocities of  $-184.2 \pm 0.3 \text{ km s}^{-1}$  and  $-26.0 \pm 0.3 \text{ km s}^{-1}$ , respectively, which are both consistent with measurements made by previous studies to suggest no radial velocity variation (HD 175305: Carney et al. 2003; Nordström et al. 2004; HD 122563: Bond 1980; Gratton & Sneden 1994; Barbay et al. 2003; Honda et al. 2004a; Aoki et al. 2005, 2007). For HD 196944, we measure a heliocentric radial velocity of  $-166.4 \pm 0.3 \text{ km s}^{-1}$ . The scatter in our radial

<sup>10</sup> Whaling et al. (2002) propose a change in the Learner & Thorne (1988) Fe I wavenumber scale, who calibrated to the absolute Ar II wavenumber scale from Norlén (1973). The proposed change, a multiplicative correction of  $1+67(8)\times 10^{-9}$ , amounts to a correction of  $\sim 0.001 - 0.002 \text{ cm}^{-1}$  or  $0.3 - 0.5 \text{ m\AA}$  in the visible spectral region examined in our study. This correction is negligible for our purposes.

velocity measurements of this star from individual observations over the very small date range 2006 June 12–18 is consistent with a single value. Lucatello et al. (2005) compiled recent radial velocity measurements for this star (ranging from  $-174.76 \pm 0.36 \text{ km s}^{-1}$ , Aoki et al. 2002 to  $-168.49 \pm 0.11 \text{ km s}^{-1}$ , Lucatello et al. 2005, see additional references therein) and concluded that it does exhibit radial velocity variations, consistent with their assertion that all carbon-enhanced, *s*-process-rich, very metal-poor stars are members of binary (or multiple) star systems. Our measurement supports the inclusion of HD 196944 in this category of stars.

#### 4.2. Equivalent Width Measurements

Our high-resolution and high-S/N observations of these stars are superior to spectra analyzed in previous studies, so we re-derive the atmospheric parameters for these stars. We combine the linelists and adopt  $\log(gf)$  values from Fulbright (2000), Honda et al. (2004a), and Ivans et al. (2006). Equivalent widths of isolated lines are measured in IRAF by fitting Gaussian profiles or by direct integration. We later discard the equivalent width measurements of lines that are approaching saturation, as indicated by their position on an empirical curve-of-growth. In each of our stars, equivalent widths are measured for  $\sim 40$ – $50$  Fe I lines,  $\sim 8$  Fe II lines,  $\sim 10$  Ti I lines, and  $\sim 7$  Ti II lines. A comparison of our equivalent width measurements with previous high-resolution studies of these reveals that there are no systematic differences in the measured equivalent widths between our study and their studies. We find mean offsets of only  $\Delta \text{EW} \equiv (\text{previous study}) - (\text{our study}) = +0.5 \pm 1.2 \text{ m\AA}$  for HD 122563 (Honda et al. 2004a),  $\Delta \text{EW} = -1.0 \pm 2.2 \text{ m\AA}$  for HD 175305 (Fulbright 2000), and  $\Delta \text{EW} = -0.8 \pm 2.3 \text{ m\AA}$  for HD 196944 (Začs et al. 1998).

#### 4.3. Atmospheric Parameters

We use Kurucz (1993) model atmospheres without convective overshooting for HD 175305 and HD 196944 and with overshooting for HD 122563 because its metallicity is beyond the range of atmospheres provided without overshooting. Interpolation software for the Kurucz grids has been kindly provided by A. McWilliam and I. Ivans (2003, private communication).

We have obtained  $V - J$ ,  $V - H$ , and  $V - K$  colors for our stars from the SIMBAD<sup>11</sup> and 2MASS<sup>12</sup> 13 (Skrutskie et al. 2006) databases. We adopt zero reddening values for these stars as recommended by previous studies (HD 122563: Honda et al. 2004b; HD 175305: Wallerstein et al. 1979; HD 196944: Zacs et al. 1998, Jonsell et al. 2005). We derive effective temperatures

for these stars using the empirical color- $T_{\text{eff}}$  calibrations given by Ramírez & Meléndez (2005), using interpolation software kindly provided by I. Ramírez<sup>14</sup>. Their work recalibrated and extended the range of color and metallicity applicability of earlier work by Alonso et al. (1996, 1999), who employed the infrared flux method to determine effective temperatures of F, G, and K dwarfs and giants. There is a rather small amount of scatter among giants in the temperature and metallicity ranges we are using (see Ramírez & Meléndez 2005’s Figure 4). The uncertainties intrinsic to the scatter of these calibrations and in the scatter of the temperatures predicted by each individual color lead us to adopt  $\pm 100 \text{ K}$  as the uncertainty in our effective temperatures.

To determine the remainder of the model atmosphere parameters we use the most recent version of the LTE spectrum analysis code MOOG (Sneden 1973). We allow for slight ( $\sim 20 \text{ K}$ ) modifications to the photometric temperatures to ensure that the abundances derived from lines with both high and low excitation potentials agree in our final atmospheric model. We derive the surface gravity by requiring that the abundances derived from neutral and ionized lines of Fe and Ti agree; we adopt  $\pm 0.3$  as the uncertainty in  $\log(g)$ . The microturbulence is measured by requiring that the abundances derived from strong and weak lines of each atomic species agree; we adopt  $\pm 0.3 \text{ km s}^{-1}$  as the uncertainty in our microturbulence. These parameters are varied iteratively until we arrive at our final values.

We employ synthetic spectra to measure the macroturbulent broadening in our stars by fitting the line profiles of  $\sim 5$ – $10$  clean Fe I and Fe II lines in each star. Uncertainties of  $0.3$ – $0.4 \text{ km s}^{-1}$  were found for the macroturbulent velocities. Our line profiles are well-fit by the convolution of the Gaussian (instrumental) and macroturbulent (stellar) broadening terms.

Our metallicity is defined to be the derived Fe I abundance, with an adopted uncertainty of  $\pm 0.15$  dex. This uncertainty represents the systematic uncertainties associated with determining  $T_{\text{eff}}$  ( $\sim 0.09$ – $0.12$  dex) and the intrinsic line-to-line scatter ( $\sim 0.10$  dex). Each of these stars are known to be  $\alpha$ -enhanced (HD 175305:  $[\alpha/\text{Fe}] = +0.3$ , Fulbright 2000; HD 196944:  $[\alpha/\text{Fe}] = +0.35$ , Zacs et al. 1998; HD 122563:  $[\alpha/\text{Fe}] = +0.4$ , Honda et al. 2004b). We have increased the overall metal abundance in our model atmosphere,  $[\text{M}/\text{H}]$ , by  $0.2$  dex relative to the Fe I abundance to account for the extra electron-donating  $\alpha$ -elements (see, e.g. Brown et al. 1991; Sneden et al. 1994)<sup>15</sup>. For elemental abundance ratios (e.g.,  $[\text{X}/\text{Fe}]$ ) measured in our study, we reference neutral species to the Fe I abundance and ionized species to the Fe II abundance.

Our final model atmosphere parameters are listed in

<sup>11</sup> This research has made use of the SIMBAD database, operated at CDS, Strasbourg, France.

<sup>12</sup> This research has made use of the NASA/ IPAC Infrared Science Archive, which is operated by the Jet Propulsion Laboratory, California Institute of Technology, under contract with the National Aeronautics and Space Administration.

<sup>13</sup> This publication makes use of data products from the Two Micron All Sky Survey, which is a joint project of the University of Massachusetts and the Infrared Processing and Analysis Center/California Institute of Technology, funded by the National Aeronautics and Space Administration and the National Science Foundation.

<sup>14</sup> Available online: <https://webpace.utexas.edu/ir68/teff/dataII.htm>

<sup>15</sup> We have performed a test to compare abundances measured from equivalent widths of Ti, Fe, and Eu using three different Kurucz model atmospheres. For a typical metal-poor star, we adopt  $T_{\text{eff}} = 5000 \text{ K}$ ,  $\log(g) = 2.0$ , and  $v_t = 2.0 \text{ km s}^{-1}$  in all three models. For atmosphere 1,  $[\text{Fe}/\text{H}] = -2.0$  and  $[\alpha/\text{Fe}] = +0.0$ . For atmosphere 2,  $[\text{Fe}/\text{H}] = -1.8$  and  $[\alpha/\text{Fe}] = +0.0$ . For atmosphere 3,  $[\text{Fe}/\text{H}] = -2.0$  and  $[\alpha/\text{Fe}] = +0.4$ . Atmospheres 1 and 2 use the Kurucz grid of  $\alpha$ -normal atmospheres, while atmosphere 3 uses the Kurucz grid of  $\alpha$ -enhanced atmospheres. The derived abundances are equivalent to within  $0.02$  dex in all cases, and this systematic effect is completely negligible for purposes of our study.

Table 1. For comparison, we show the atmospheres derived in previous studies of these stars. Table 1 indicates that our atmospheric parameters are in good agreement with these studies.

#### 4.4. Line Profile Analysis

To measure the isotopic fractions, the observed absorption lines are fit by synthetic spectra. Although our line lists are initially generated from the extensive lists of Kurucz & Bell (1995)<sup>16</sup>, we employ experimental wavelengths and  $\log(gf)$  values for all lines of interest and blended features whenever possible. Our Eu, Sm, and Nd lines are synthesized by accounting for the individual hyperfine and isotopic components; the isotope fraction and elemental abundance are varied to provide a best fit to the observed profiles.

At the spectral resolution employed in this study, some of our unblended Fe I and II lines exhibit a slight profile asymmetry. This observation is consistent with our assumption that the macroturbulent velocity arises, at least in part, from large-scale convective motions in the stellar photosphere. These asymmetries account for  $\approx 1$ –2% of the total equivalent width of the line, and the typical bisector amplitude is  $\approx 200$ –300  $\text{m s}^{-1}$ . The shapes of our line bisectors are consistent with those observed for K giants, e.g., Arcturus, by Dravins (1987). We have not explored any attempts to introduce 3D modeling of the stellar atmospheres into our analysis; such models are not yet available for metal-poor giant stars. In this study we restrict ourselves to the use of one-dimensional, plane-parallel model atmospheres computed for the LTE case.

In contrast to the challenge of detecting the presence of  $^6\text{Li}$  from the Li I 6707Å line profile, which likely requires 3D-NLTE modeling to account for the convective asymmetry that can mimic the presence of  $^6\text{Li}$  (Cayrel et al. 2007), the change in the line profile that we analyze is very different. The presence of the  $^6\text{Li}$  component may account for only a few tenths of a percent of the total flux in the red wing of the  $^7\text{Li}$  line, which is a very subtle effect. The magnitude of the HFS for Eu causes gross changes in the shape of the entire line profile (see § 6.1). Sm and Nd each have seven naturally-occurring isotopes, so the shape of the line profile will be asymmetric along all parts of the line and not just along the red wing where convective asymmetries are most prominent. Therefore our choice to compute 1D synthetic line profiles in LTE will not significantly affect our results for these species.

##### 4.4.1. Detailed Examination of the Absorption Line Profile

Isotope shifts and HFS alter the shape of the line profile, and the isotopic fraction can be assessed by examining the line profile from detailed comparisons between the observed and synthetic spectra. This method has been used previously to assess the Eu isotopic fraction by Sneden et al. (2002) and Aoki et al. (2003a,b). We quantify our measurements of the isotopic fractions using a  $\chi^2$  algorithm (after, e.g., Smith et al. 2001; Aoki et al. 2003a; Asplund et al. 2006),

$$\chi^2 = \left\langle \frac{(O_i - C_i)^2}{\sigma_i^2} \right\rangle. \quad (4)$$

Here  $O - C$  is the difference between the observed and synthetic spectra at the  $i$ th spectrum point and  $\sigma$  is defined as  $\sigma_i = [(S/N) \times (f_i)^{1/2}]^{-1}$ , where S/N is the approximate signal-to-noise ratio of the continuum and  $f$  is the depth of the  $i$ th point relative to the continuum. Our best estimate of the isotopic fraction and abundance for each line is given by minimizing  $\chi^2$ . Uncertainties are estimated at 1, 2, and 3  $\sigma$  confidence intervals from  $\Delta\chi^2 = \chi^2 - \chi_{min}^2 = 1, 4,$  and 9, respectively. We consider the number of degrees of freedom in the fit to be the number of points in the spectral window plus the continuum normalization, abundance, and wavelength offset, all of which were allowed to vary in our fits. Reduced  $\chi^2$  values are  $\sim 1$ , differing by less than a factor of two, which is still larger than would be expected for a normal distribution of errors (e.g., Press et al. 1992). We attribute the scatter in the reduced  $\chi^2$  values to our estimation of the S/N ratio. The *relative*  $\chi^2$  values for a given line, represented by  $\Delta\chi^2$ , however, do exhibit well-determined minima. We fix the macroturbulence, as determined in § 4.3, but we also estimate the uncertainties in the isotopic fraction introduced by the uncertainty in the macroturbulence,  $V_{macro} \pm \Delta V_{macro}$ . Only our Eu and Sm lines with complete sets of hyperfine constants (see § 3) can be assessed by this method.

##### 4.4.2. Set the Absolute Wavelength Scale from Nearby Wavelength Standards

In principle, the absolute wavelengths of the observed and synthetic spectra can be matched using wavelength standard Fe I and Ti II lines, and then the peak wavelength of the rare-earth line of interest can be measured. The isotopic fraction can be assessed because the isotope shifts—much more than the HFS—affect the peak absorption wavelength. Lundqvist et al. (2007) have used this method to qualitatively demonstrate that the Sm isotopic mix in CS 31082-001 is consistent with an  $r$ -process origin.

For our Sm lines, a small wavelength shift ( $\sim 0.02$ – $0.04\text{Å}$ ) is the dominant effect of changing the isotopic fraction; for our Nd lines, the shift is even smaller ( $\sim 0.01\text{Å}$ ). In both cases, broadening of the line profile is a secondary effect. Therefore, given the small magnitudes of these shifts, it is critical that we match the wavelength scales of our synthetic and observed spectra with great accuracy. The absolute wavelengths of some of our Sm HFS components are accurate to  $\pm 1 \text{ mÅ}$ , as determined by the FTS measurements of  $^{154}\text{Sm}$  by Lundqvist et al. 2007 (see Appendix B), while the absolute wavelengths of the Sm lines not included in that study are accurate to  $\approx 2 \text{ mÅ}$ . Unlike Sm, however, the atomic data for Nd does not include FTS measurements of individual isotope positions, so our reported absolute wavelengths of Nd components are based solely on measurements of the Nd energy levels. To avoid mixing measurements of energy levels from different studies, we adopt the energy levels from Blaise et al. (1984). They estimate an uncertainty of  $\pm 0.005 \text{ cm}^{-1}$  for each level. Doubling this uncertainty translates to an uncertainty of  $\sim 1.5$ – $2.0 \text{ mÅ}$  across the region where our Nd lines are located. We note that the relative HFS component wavelengths—measured from FTS spectra—are more accurate than this in all cases. The absolute wavelengths of

<sup>16</sup> Available online: <http://kurucz.harvard.edu/linelists.html>

the wavelength standard lines (Fe I: Learner & Thorne 1988 and Nave et al. 1994; Ti II: Pickering et al. 2001, 2002) have a reported absolute accuracy in their FTS measurements of  $\sim \pm 0.001 \text{ cm}^{-1}$  ( $\lesssim 0.3 \text{ m}\text{\AA}$ ) in our wavelength regions. The uncertainties from our wavelength scale and co-addition of individual orders are no larger than  $\pm 0.9 \text{ m}\text{\AA}$ , and we have verified that, after the wavelength solution has been applied, the Th-Ar emission lines are correctly identified to within  $\sim \pm 1 \text{ m}\text{\AA}$ . All of these uncertainties are sufficiently small to enable reliable measurement of the isotopic fraction.

In each echelle order containing a rare-earth line of interest, we locate 1–6 wavelength standard lines and match the wavelength scales of the observed and synthetic spectra at each of these lines, typically with a precision of  $\sim 1 \text{ m}\text{\AA}$  per line. When multiple wavelength standards are used, the scatter in our measured wavelength offsets necessary to ensure the matching of each line is  $\sim 5 \text{ m}\text{\AA}$ , much greater than anticipated. This scatter appears to be independent of the ionization state, species, excitation potential, and relative strength of the wavelength standards, each of which could be expected to introduce small systematic offsets among lines with these different characteristics (see, e.g., Dravins et al. 1981, 1986; Asplund et al. 2000). The isotopic fraction we would derive from our rare-earth lines of interest is therefore entirely dependent upon our choice of which wavelength standard line(s) we adopt and how many of these lines are present in the echelle order with the rare-earth line.

To further understand this matter, we have also attempted to match the observed and synthetic spectra for wavelength standards in the Solar spectrum. We compare both the Kurucz et al. (1984) integrated-disk Solar spectrum, obtained with the FTS on the McMath Solar Telescope at Kitt Peak National Observatory, and daylight sky spectra, obtained using the same instrumental configuration on the McDonald Observatory 2dCoudé echelle spectrograph as our stellar observations and reduced in an identical fashion. It is well-known that astronomical echelle spectrographs and cameras can introduce a variety of non-linear distortions to the wavelength scale, whereas the spectrum obtained with the FTS should be immune to many of these distortions. We synthesize a spectral region from 4997–5010 Å (one echelle order) using an interpolated Holweger & Müller (1974) empirical Solar model photosphere. We apply our matching technique to the five unblended Fe I wavelength standard lines in common to the two spectra. We measure the same line-to-line wavelength offsets for these lines in both spectra (agreement within our measurement precision,  $\sim 1 \text{ m}\text{\AA}$ ), suggesting that the wavelength scale of our 2dCoudé spectra is consistent with the Kitt Peak FTS spectra. Nevertheless, the scatter in the absolute wavelength scale as determined from each of these lines in the FTS spectrum is *still*  $\sim 5 \text{ m}\text{\AA}$ , indicating that there is a more fundamental problem that does not result from our spectral reduction techniques or our ability to match the observed and synthetic spectra. Unable to further identify and quantify the source of this discrepancy, we are unable to proceed with confidence by this method of analysis.

#### 4.4.3. Set the Relative Wavelength Scale at the Point of Insensitivity to the Isotopic Mix

We also develop one additional method of quantifying the isotopic fraction that does not rely on nearby wavelength standard lines or fits to the shape of the line profile. The reason for developing such a method is our desire to assess the isotopic mix from all lines with maximum isotopic shifts  $\gtrsim 15 \text{ m}\text{\AA}$  and from which an elemental abundance can be measured. This allows us to examine additional Sm lines that do not have full sets of measured hyperfine A and B constants as well as all of the Nd lines.

This method attempts to match the observed and synthetic spectrum using the point in the synthetic spectrum that is insensitive to the *s*- or *r*-process mix. First, for each line, an isotopic fraction is assumed in the synthesis, and we always adopt  $f = 0.50$  by default. Then an elemental abundance is derived from a synthesis with this isotopic fraction. Using this elemental abundance, two new syntheses (one with a pure-*s*-process mix of isotopes and one with a pure-*r*-process mix) are created. The intersection of these two syntheses is defined to be the point of insensitivity to the isotopic fraction. The relative wavelength offset between the point of insensitivity and the observed spectrum is then adjusted until the point of insensitivity is coincident with the flux of the nearest pixel of the observed spectrum. Next, we adopt this relative wavelength offset and generate a set of synthetic spectra with a range of isotopic fractions but the same elemental abundance. A new isotopic fraction is then measured by minimizing the sum of the squares of the differences between the observed and synthetic spectra. This isotopic fraction is then used as the input to derive an elemental abundance, and the process is repeated until the elemental abundance and isotopic fraction have each converged. We show an example where the point of insensitivity has been matched to the observed spectrum in Figure 2.

The uncertainty in the matching process is given by the width of one pixel; therefore the uncertainty in the derived isotopic fraction is estimated by shifting the synthetic spectrum relative to the observed spectrum by  $\pm w_{\text{pixel}}/2$ . Even at a spectral resolution of  $R \sim 120,000$ , the width of one pixel is still a substantial fraction of the width of the absorption line itself. This method also places a disproportionate amount of weight on the one or two flux measurements closest to the point of insensitivity, rather than taking account of the information from the full width of the line to match the observed and synthetic spectra. The precision achieved by this method is hardly adequate to clearly assess the isotopic mix—particularly for Nd—but it does provide a consistent set of measurements for all of our lines of Sm and Nd.

## 5. NEUTRON-CAPTURE ELEMENTAL ABUNDANCES

Our mean elemental abundance of Eu in HD 175305,  $[\text{Eu}/\text{Fe}] = +0.46 \pm 0.07$ , is in good agreement with Fulbright (2000)’s abundance,  $[\text{Eu}/\text{Fe}] = +0.48 \pm 0.105$ , and Cowan et al. (2005)’s abundance,  $[\text{Eu}/\text{Fe}] = +0.55 \pm 0.10$ . Our synthesis of the Eu II 4205 Å line in HD 122563 does permit measurement of the Eu elemental abundance,  $[\text{Eu}/\text{Fe}] = -0.55 \pm 0.06$ , assuming  $^{12}\text{C}/^{13}\text{C} = 5$

(Lambert & Sneden 1977; Honda et al. 2004b) and a Eu isotopic fraction of  $f_{151} = 0.5$ . The Eu abundance changes by  $\pm 0.03$  dex when the assumed isotopic ratio is varied by  $\pm 0.2$  dex. This elemental abundance agrees very well with the value found by Honda et al. (2006),  $[\text{Eu}/\text{Fe}] = -0.52$ , and with many previous studies of this star. The 4205Å line in HD 196944 is far too sensitive to the C abundance to derive a meaningful Eu elemental abundance.

We measure Sm elemental abundances of  $[\text{Sm}/\text{Fe}] = -0.56 \pm 0.12$  from 1 line in HD 122563,  $[\text{Sm}/\text{Fe}] = +0.37 \pm 0.11$  from 9 lines in HD 175305, and  $[\text{Sm}/\text{Fe}] = +0.88 \pm 0.08$  from 6 lines in HD 196944. Previous studies of Sm elemental abundances in these stars have found  $[\text{Sm}/\text{Fe}] = -0.40 \pm 0.17$  in HD 122563 (Honda et al. 2006) and  $[\text{Sm}/\text{Fe}] = +0.78 \pm 0.23$  in HD 196944 (Aoki et al. 2002); Sm has not been measured previously in HD 175305. Unlike the uncertainties in the isotopic fractions, the uncertainties in the elemental abundances are dominated by the systematic uncertainties in the model atmosphere parameters and are affected somewhat less by internal scatter from the  $\log(gf)$  values.

We measure Nd elemental abundances of  $[\text{Nd}/\text{Fe}] = +0.22 \pm 0.13$  from 12 lines in HD 175305 and  $[\text{Nd}/\text{Fe}] = +0.95 \pm 0.13$  from 11 lines in HD 196944. Previous studies of Nd elemental abundances in these stars have found  $[\text{Nd}/\text{Fe}] = +0.34$  (Burriss et al. 2000) in HD 175305 and  $[\text{Nd}/\text{Fe}] = +0.93 \pm 0.09$  (Van Eck et al. 2001),  $[\text{Nd}/\text{Fe}] = +0.94 \pm 0.17$  (Začs et al. 1998), and  $[\text{Nd}/\text{Fe}] = +0.86 \pm 0.20$  (Aoki et al. 2002) in HD 196944.

We have also measured elemental abundances for five additional heavy  $n$ -capture elements in HD 175305. These abundances are listed in Table 3 along with our Eu, Sm, and Nd abundances. The uncertainties listed in the table reflect the uncertainties in the atmospheric parameters, continuum placement, line-to-line scatter, and  $\log(gf)$  values, all added in quadrature. In cases where only one line of a species was available for analysis, we substitute the uncertainty in the spectral synthesis fit to the observed spectrum in place of the line-to-line statistical scatter in this formula. In Figure 3 we plot our elemental abundances, combined with measurements from Fulbright (2000), Cowan et al. (2005), and Lawler et al. (2007), against the scaled S. S.  $r$ -process abundance pattern of Simmerer et al. (2004). While not a perfect fit, this figure suggests that the scaled S. S.  $r$ -process abundance pattern provides a respectable fit of the observed  $n$ -capture abundances beyond Ba. HD 175305 may not be a star with pristine  $r$ -process material, but the  $r$ -process appears to have contributed the majority of the  $n$ -capture species present. We have also used the Keck I HIRES spectrum of HD 175305, obtained for the Cowan et al. (2005) study, to determine an upper limit for Pb from the 4057Å line.

## 6. NEUTRON-CAPTURE ISOTOPIC FRACTIONS

We emphasize that measurements of isotopic fractions are highly insensitive to the choice of atmospheric parameters. Separate isotopic components of a line all share the same initial and final energy levels (since the HFS of these levels is negligible relative to the energy differences themselves), eliminating systematic errors associated with the excitation and ionization states of each isotope.

### 6.1. The Europium Isotopic Fraction

#### 6.1.1. In the Sun

For S. S. material, the  $n$ -capture isotopic abundances are precisely known from studies of terrestrial meteorites. The Eu II isotopic fraction in the Solar spectrum was first studied by Hauge (1970) and Hauge (1972), who found  $^{153}\text{Eu}/^{151}\text{Eu} = (48 \pm 6)/(52 \mp 6)$  (or  $f_{151} = 0.52$  in our notation). Lawler et al. (2001b) reevaluated the Solar Eu isotopic fraction, finding  $f_{151} = 0.50 \pm 0.07$  from the 4129Å line. We do not repeat this measurement here.

#### 6.1.2. In Metal-Poor Stars

From the Eu II 4129Å line in HD 175305 we measure an isotopic fraction of  $f_{151} = 0.50 \pm 0.04$ , as shown in Figure 4. The  $\Delta\chi^2$  values are shown in Figure 5 for different values of the isotopic fraction and macroturbulent velocity. The minimum  $\Delta\chi^2$  values have well-defined minima, leading to the small uncertainties in the derived isotopic fraction. As noted in Appendix A.1, we cannot trust our syntheses of the Eu II lines at 4205 and 4435Å at the precision necessary to measure an isotopic fraction. For the sake of comparison, in Figures 6 and 7 we show our synthesis of these two lines in HD 175305 given our best estimate of the blending features, but we emphasize that these syntheses display the best-fit isotopic fraction derived from the 4129Å line.

The Eu II 4129Å line was not covered in our spectra of either HD 196944 or HD 122563.

Although only two naturally-occurring isotopes of Eu exist, only a small spread is predicted between  $f_{151}^s$  and  $f_{151}^r$  (see panel **a** of Figure 4). It is difficult even with very high-resolution ( $R \gtrsim 100,000$ ) and high-S/N ( $\sim$  few hundred) data on one or more lines to achieve sufficiently small uncertainties on isotopic abundances to determine the nucleosynthetic source of the Eu. Sneden et al. (2002); Aoki et al. (2003a,b) have successfully shown that the Eu  $s$ - and  $r$ -process nucleosynthetic signatures can be distinguished at the isotopic level, using approximately three lines in each of seven stars. The measurements made from individual lines in each star in these studies have a large degree of scatter, causing the final Eu isotopic fraction to be mildly sensitive to the set of lines chosen. For example, we note that Aoki et al. (2003a)'s two measurements of  $f_{151}$  from the 4435Å line appear systematically higher than the results obtained from the 4205Å line by  $\approx 10$ –15%, which is roughly the same as the change in the Eu isotopic fractions that are trying to be distinguished. Although we do not measure an isotopic fraction from the 4435Å line in HD 175305, our syntheses hint at a similar result in the small region without obvious blends (4435.40–4435.50Å). Additional measurements of the Eu isotopic fraction from these lines would be helpful to confirm or refute these possible systematic trends. If such systematic trends exist, they likely result from the presence of blending features, and the measured isotopic fractions may be as sensitive to the blending features as to the Eu isotopes themselves. There is little hope of being able to distinguish Eu isotopic fractions with any greater precision than has already been achieved using these methods on this set of lines, including the Eu II lines at 3819 and 3907Å.

## 6.2. The Samarium Isotopic Fraction

### 6.2.1. In the Sun

Ekeland & Hauge (1975) analyzed the Sm isotopic fraction in the Solar photosphere from two lines, 4467 and 4519Å, finding isotopic fractions consistent with the meteoritic values. The 4467Å line is broadened slightly by HFS, with almost zero broadening resulting from the isotope shifts, while the 4519Å line is broadened slightly by isotope shifts. High-precision single-frequency laser measurements of the isotope shifts for  $^{147}\text{Sm}$  and  $^{149}\text{Sm}$  have not been measured in the lab for the 4519Å line, therefore we do not attempt synthesis of this line.

We synthesize the 4467Å line using the Holweger & Müller (1974) model atmosphere and the Kurucz et al. (1984) Solar spectrum. We fix the broadening from nearby Fe lines. The total spread in the HFS and isotope shifts for this line are  $\lesssim 0.05\text{Å}$  and  $\lesssim 0.01\text{Å}$ , respectively, and we cannot measure the isotopic fraction, either in terms of  $f_{\text{odd}}$  or  $f_{152+154}$ , from the line-profile-fitting method even when a high-quality Solar spectrum is used. Ekeland & Hauge (1975) provide very little information about their method of measuring the Sm isotopic fraction, and their very small uncertainties ( $f_{\text{odd}} = 0.28 \pm 0.07$ ) for a line with relatively small HFS and isotope shifts give us some reservation in accepting their result. All of the other Sm transitions listed in Appendix A.2 are either far too weak or are severely-blended with strong transitions of other species to measure reliable isotopic fractions in the Solar spectrum, so we are unable to make any measurements of the Sm isotopic fraction in the Solar photosphere. We remind the reader that the blended lines may be reliable for measurements of the Sm elemental abundance, but we cannot trust our syntheses of the blending features at a precision necessary to measure isotopic fractions.

### 6.2.2. In Metal-Poor Stars

Figures 8 and 9 show our syntheses of the Sm II line at 4424Å in HD 175305 and HD 196944, respectively, and the results from our line profile fits. We also include the Cr abundance of the Cr I 4424.28Å line, which blends the blue wing of the Sm line, as a free parameter. In HD 122563, this Sm line has a relative depth of  $\sim 2\%$ . We do not claim measurements of either the elemental abundance or isotopic fraction of Sm from this line in HD 122563; it is clear that this line is simply too weak to warrant further analysis. In HD 175305, we measure a Sm isotopic fraction of  $f_{152+154} = 0.55 \pm 0.14$ . In HD 196944, we measure a Sm isotopic fraction of  $f_{152+154} = 0.35^{+0.11}_{-0.20}$ . In addition to showing the best fit curves and their uncertainties in Figures 8 and 9, we also show the syntheses for pure-*s*- and pure-*r*-process nucleosynthesis and the (*O* - *C*) curves for these syntheses, illustrating the contrast between the two extremes. In each of these figures, the pure-*s*- and pure-*r*-process syntheses in panel **b** are compared to the observed spectra in panel **a**, illustrating the degree to which the observed spectrum tends toward one synthesis or the other.

Figure 10 shows our synthesis of the Sm II line at 4604Å in HD 175305. We measure a Sm isotopic fraction of  $f_{152+154} = 0.50^{+0.09}_{-0.14}$ . This line is weak, with a relative depth of only 5%. Figure 11 shows the  $\Delta\chi^2$  values for

our fit to this line;  $\Delta\chi^2$  values from the Sm 4424Å line in both stars are similar to the 4604Å line.

If instead we match the observed and synthetic spectra at the point of insensitivity to the isotopic fraction, we find  $f_{152+154} = 0.41 \pm 0.32$  from the 4424Å line,  $f_{152+154} = 0.49 \pm 0.17$  from the 4604Å line, and  $f_{152+154} = 0.49 \pm 0.20$  from the 4719Å line in HD 175305. In HD 196944, we find  $f_{152+154} = 0.37 \pm 0.28$  from the 4424Å line. While we regard the line profile fits as the superior measurements of the isotopic fraction, the agreement between the sets of measurements from the two methods is reassuring.

## 6.3. The Neodymium Isotopic Fraction

### 6.3.1. In the Sun

We check our Nd isotopic fraction measurements against the Solar spectrum. We are aware of no previous attempts to examine the Nd isotopic mix in the Solar photosphere, but the individual S. S. isotopic abundances have been established from studies of terrestrial meteorites. The Nd II line at 4446Å would appear to be the most reliable indicator of the Nd isotopic fraction due to its relative strength and freedom from blending features. The line profile shape does not change enough to allow us to apply our fitting algorithm to measure the isotopic fraction, and we can find no good candidate Fe I or Ti II lines nearby to match the observed and synthetic spectra. By using the method of matching the observed and synthetic spectra at the point of insensitivity to the isotopic mix, we derive an isotopic fraction of  $f_{142+144} = 0.53^{+0.47}_{-0.53}$ , which is unfortunately unable to exclude any possible combination of isotopes. Therefore, we are unable to provide independent confirmation of the S. S. Nd isotopic fraction from analysis of the Solar photosphere.

### 6.3.2. In Metal-Poor Stars

Because the isotope shifts of Nd are smaller than Sm and because we cannot match our observed and synthetic spectra with a high absolute accuracy, we can only rely on the third matching method to measure the isotopic fraction of the Nd lines in these stars. In HD 175305, we measure  $f_{142+144} = 0.25^{+0.75}_{-0.25}$  from the 4177Å line,  $f_{142+144} = 0.11^{+0.85}_{-0.11}$  from the 4446Å line, and  $f_{142+144} = 0.33^{+0.67}_{-0.33}$  from the 4567Å line. The mean isotopic fraction of these three lines is  $f_{142+144} = 0.21^{+0.56}_{-0.21}$ . Combining these measurements together using the asymmetric uncertainties that reflect the fact that the isotopic fraction cannot be less than 0.0 or greater than 1.0 could introduce a bias into the weighted mean. Therefore we have estimated the uncertainties in these measurements also by assuming (non-physically) that the isotopic fraction can exceed these limits. We find uncertainties of  $\pm 1.10$ ,  $\pm 0.85$ , and  $\pm 1.00$  on these three lines, respectively, resulting in a weighed uncertainty of  $\pm 0.56$  on the mean. Our final quoted uncertainties do impose the physical limits on the isotopic fractions. In HD 196944, we measure  $f_{142+144} = 0.36^{+0.64}_{-0.36}$  from the 4446Å line. The non-physical uncertainty on this measurement is  $\pm 0.68$ , which provides a relative comparison to our ability to measure the 4446Å line in HD 175305.

Unfortunately none of these individual measurements provides any real insight into the Nd isotopic fraction due to the size of the uncertainties. The large uncertainties also prevent us from pointing out even a contrast between the Nd isotopic mixes in the two stars, much less make any detailed assessment of the  $s$ -process nucleosynthetic predictions.

#### 7. INTERPRETATION OF THE NUCLEOSYNTHETIC SIGNATURES

In HD 175305, our Sm isotopic fraction  $f_{152+154} = 0.51 \pm 0.08$ , a weighted average of our measurements from profile fits to the 4424 and 4604Å lines, suggests an  $r$ -process origin. It is tempting to surmise that our Nd isotopic fraction,  $f_{142+144} = 0.21_{-0.21}^{+0.56}$ , derived from three lines, is suggestive of an  $r$ -process origin, but the large uncertainty cannot exclude an  $s$ -process origin. Our Eu isotopic fraction,  $f_{151} = 0.50 \pm 0.04$ , derived from only the 4129Å line and shown to be a reasonable match for the 4205 and 4435Å lines, implies an  $r$ -process origin by the Cowan et al. (2006) predictions but excludes neither a pure- $s$ - nor a pure- $r$ -process origin by the Arlandini et al. (1999) predictions. It is interesting to note that our isotopic fractions in HD 175305 suggest a nucleosynthetic history predominantly—but perhaps not purely—dominated by the  $r$ -process, which also is suggested by the elemental abundance trends. The fact that both the elemental and the isotopic distributions in HD 175305 agree with the predicted elemental and isotopic distributions of  $r$ -process material in the S. S. adds to the preponderance of evidence that supports the hypothesis of a universal  $r$ -process mechanism for elements with  $Z \geq 56$ .

In HD 196944, our measured Sm isotopic fraction,  $f_{152+154} = 0.35 \pm 0.14$ , is suggestive of an  $s$ -process origin. Our Nd isotopic fraction,  $f_{142+144} = 0.36_{-0.36}^{+0.64}$  can exclude no possible values of the isotopic mix. The interpretation for the Sm is consistent with the  $s$ -process elemental abundance signatures and radial velocity variation described in § 4.1.

Our best measurements for each species are summarized in Figures 12 and 13 for both HD 175305 and HD 196944. In Figure 12, the differences between the pure- $r$ - and pure- $s$ -process predictions are scaled together to emphasize the relative precision with which the two processes can be distinguished by each species. In contrast, Figure 13 displays our measurements in an absolute sense to emphasize the relative precision with which each species was measured. Expressed this way, it is clear that Eu can be measured precisely but does not easily reveal its nucleosynthetic origin because of the small difference between  $f_{151}^r$  and  $f_{151}^s$ . The uncertainties on each Nd line can hardly exclude any possible value of the isotopic fraction. Only the Sm isotopic fractions, which have uncertainties on the individual measurements that are smaller than the difference between  $f_{152+154}^r$  and  $f_{152+154}^s$ , offer any opportunity to distinguish the two processes with reasonable precision.

#### 8. EU/PB AND $^{151}\text{EU}/\text{PB}$ ABUNDANCE RATIOS

In § 3.2 we pointed out the great discrepancy between the stellar model of Arlandini et al. (1999) and the classical method of Cowan et al. (2006) in predicting the amount of  $^{151}\text{Eu}$  produced by the  $s$ -process:

$N_s = 0.00304 \pm 0.00013$  and  $N_s = 0.0001$ , respectively. The stellar model predicts that the  $s$ -process should produce  $\sim 30$  times more  $^{151}\text{Eu}$  than the classical method does. For a certain amount of  $^{151}\text{Eu}$  produced by an  $s$ -process nucleosynthesis event, the classical method would then predict that the isotopes near the termination of the  $s$ -process—such as Pb—should be overproduced by a factor  $\sim 30$  relative to the stellar model.

We choose Pb for this comparative analysis because it is so dominantly produced by the  $s$ -process. In Pb-enriched metal-poor stars, such as HD 196944, the Pb overabundance often will reach  $[\text{Pb}/\text{Fe}] \geq +2.0$ , making it easy to detect at the Pb I 4057Å transition. Because Eu is produced more easily by the  $r$ -process than by the  $s$ -process (relatively speaking) and Pb is produced more easily by the  $s$ -process than by the  $r$ -process, the Eu/Pb and  $^{151}\text{Eu}/\text{Pb}$  abundance ratios in metal-poor stars should be extremely good discriminators of the predicted abundances of these species.

Arlandini et al. (1999) do not predict pure- $r$ -process Pb abundances due to the fact that Pb can be overproduced relative to the lighter- $s$ -process nuclei in low metallicity AGB stars. In other words, at lower metallicity a greater number of neutrons is captured per Fe-peak seed than at higher metallicity, so the  $s$ -process abundance distribution at low metallicity favors the heaviest  $s$ -process nuclei; see, e.g., Gallino et al. (1998), Busso et al. (1999), and Straniero et al. (2006).

In Figure 14 we have compiled the derived Eu/Pb ratios (or upper limits) for 35 metal-poor stars from a variety of recent studies and for HD 175305. The Eu/Pb ratio shows no obvious trends when expressed as a function of  $[\text{Fe}/\text{H}]$ , but we note that this sample of Eu and Pb abundances is far from complete. Adopting the original authors' classifications for the enrichment patterns for these stars, this sample consists of 6  $r$ -process-enriched stars (Cowan et al. 2002; Hill et al. 2002; Aoki et al. 2003a; Sneden et al. 2003; Plez et al. 2004; Ivans et al. 2006; Frebel et al. 2007; A. Frebel, 2007, private communication), 15  $s$ -process-enriched stars (Aoki et al. 2001, 2002; Johnson & Bolte 2002; Cohen et al. 2003; Barbuy et al. 2005; Cohen et al. 2006; Preston et al. 2006), and 5 ( $r+s$ )-process-enriched stars (Ivans et al. 2005; Aoki et al. 2006; Jonsell et al. 2006; Masseron et al. 2006) from the Galactic halo population. The  $r$ -process-enhanced sample also includes 10 stars from the metal-poor globular clusters M 13 and NGC 6752 (Yong et al. 2006). The small number of  $r$ -process enriched stars results from the observational difficulty of detecting Pb in stars without  $s$ -process enrichment. The Eu/Pb ratios of the  $r$ -process-enhanced halo stars and globular cluster stars all suggest that the  $r$ -process predictions are correct. Despite the fact that  $\log \varepsilon(\text{Eu}/\text{Pb})_s$  differs by  $\sim 0.6$  dex between the stellar model and classical method predictions, the measured abundance spread in the  $s$ -process-enriched stars is still too great to unambiguously distinguish the two predictions from this information alone. The  $s$ - and ( $r+s$ )-enhanced classes of stars show little difference from one another when their Eu and Pb abundances are expressed this way.

In Figure 15 we have compiled a subset of 7 of these stars with measured Eu isotopic fractions, and we plot

log  $\varepsilon(^{151}\text{Eu}/\text{Pb})$  as a function of metallicity. This subset includes 5  $r$ -process-enhanced stars and 2 ( $r + s$ )-process-enhanced stars. Again, the  $r$ -process-enhanced halo stars cluster around the  $r$ -process predictions. Here, though, the stellar model and classical method predictions for log  $\varepsilon(^{151}\text{Eu}/\text{Pb})$  differ by  $\sim 1.7$  dex, and the two  $r+s$  stars with measured Eu isotopic fractions clearly favor the Arlandini et al. (1999) predicted  $^{151}\text{Eu}$  abundance. This is not unexpected, given that Aoki et al. (2003a), who measured the Eu isotopic fraction in these two stars, reported that  $f_{151}$  was consistent with the Arlandini et al. (1999) predictions.

It is worth considering whether these  $r + s$  stars may have enough  $r$ -process enrichment to give them a log  $\varepsilon(^{151}\text{Eu}/\text{Pb})$  abundance that lies between the Cowan et al. (2006) pure- $s$  and pure- $r$  predictions, inadvertently suggesting the Arlandini et al. (1999) value. To investigate this matter, in Figure 16 we plot the log  $\varepsilon(\text{Ba}/\text{Nd})$  abundance ratios for the full sample of halo stars; Yong et al. (2006) did not measure Ba or Nd abundances in their globular cluster stars. While there is still a relatively large amount of scatter among the  $s$ - and ( $r+s$ )-enriched stars, neither population appears distinct from the other, and the two  $r+s$  stars shown in Figure 15 scatter above and below the predicted pure- $s$ -process abundance value. We therefore conclude that these two stars are representative of predominantly- $s$ -process-enriched material, and these observations thereby support the Arlandini et al. (1999)  $^{151}\text{Eu}$  abundance prediction. We caution that this conclusion hinges on the Eu isotopic fraction measured in only two stars, and additional observations of the Eu isotopic fraction in  $s$ -process-enriched stars would be most helpful to further resolve the matter.

Straniero et al. (2006) show that in low-metallicity stars in the TP-AGB phase the abundance ratios of nuclei near the first and second  $s$ -process peaks are only weakly affected by the efficiency of the  $^{13}\text{C}$  pocket (and hence the neutron source for the  $s$ -process), whereas abundances of species near the third  $s$ -process peak are strongly dependent on this parameter. Therefore the abundance predictions of the Arlandini et al. (1999) stellar model, which was computed for  $\sim$  Solar metallicity stars in the TP-AGB phase, should predict the lighter  $s$ -process abundances at low metallicity better than it predicts the Pb abundance at low metallicity. In a low-metallicity  $s$ -process nucleosynthesis event, we would expect the  $^{151}\text{Eu}/\text{Pb}$  ratio to decrease relative to a higher-metallicity case as a higher fraction of seed nuclei are converted to Pb. Therefore, the stellar model pure- $s$  Eu/Pb and  $^{151}\text{Eu}/\text{Pb}$  ratios should represent upper limits for these values. In both cases, decreasing these ratios would bring the stellar model predictions into better agreement with the classical method predictions.

## 9. PROSPECTS FOR FUTURE STUDIES OF NEUTRON-CAPTURE ISOTOPIC FRACTIONS

Previous studies have demonstrated that the Eu and Ba isotopic fractions can be measured, we have shown that Sm isotopic fractions can also be quantitatively measured, and we also suggest that Nd isotopic fractions can be measured, albeit with lower precision than the other rare-earth species. The measurements of each set of isotopes give an indication of the stellar nucleosynthetic his-

tory that is consistent with other indicators, and we now discuss the role that measurements of Ba, Nd, Sm, Eu, and other  $n$ -capture isotopic fractions might play in future studies.

### 9.1. Isotopic Fractions of Multiple Neutron-Capture Species

It is a success of both the stellar model and classical method that these models' predictions of the Sm  $f_{152+154}$  isotopic fraction are in good agreement. Suppose that both Sm isotopic fractions  $f_{152+154}$  and  $f_{\text{odd}}$  could be measured from the same set of lines. This would enable a comparison of the models' predicted abundances of  $^{147}\text{Sm}$ , which differs by a factor of  $\sim 3$  and affects the predicted  $f_{\text{odd}}$  values, whereas both models generally agree on  $^{149}\text{Sm}$ ,  $^{152}\text{Sm}$ , and  $^{154}\text{Sm}$ . One could measure the isotopic fractions of Sm and Ba in an  $r$ -enriched star. If a convincing argument could be made that the Ba and Sm should have originated from the same nucleosynthetic event(s) (i.e., an extra contribution has not been made to the Ba abundances by another  $n$ -capture process), the isotopic fractions measured for both Ba and Sm should show the same relative proportion of  $r$ -process isotopes. This scenario could permit a direct test to the predicted Ba isotopic fractions, which differ by 26% in their  $r$ -only predictions for  $f_{\text{odd}}$ , with the most significant differences arising in the models' predictions for  $^{137}\text{Ba}$  and  $^{138}\text{Ba}$ . Such tests would be greatly welcomed.

It is not obvious why Ba abundances are sometimes larger than the scaled S. S.  $r$ -process abundances (scaled to the heavier  $n$ -capture elements) in metal-poor stars with an  $r$ -only chemical signature and no evidence of binarity, such as HD 175305. (See also, e.g., Figure 15 of Honda et al. 2004a or Figure 15 of Barklem et al. 2005, where some of their  $r$ -enriched stars exhibit this behavior.) Asplund (2004) suggests that the 3D Ba abundance correction may be as much as  $-0.5$  dex for some metal-poor dwarfs and subgiants. While this matter may indeed be a result of poor Ba abundance determinations due to 1D LTE modeling or to uncertainties in the S. S. abundance predictions, the search for an astrophysical explanation for this phenomenon should be explored further. Measurements of Ba and other  $n$ -capture isotopic fractions could be used to identify any correlations that may exist between super- $r$ -process Ba abundances and other nucleosynthetic signatures.

The combination of Ba, Nd, Sm, and Eu isotopic fractions could provide more complete knowledge of abundances at the isotopic level over a range of  $\sim 20$  mass numbers ( $A = 134-154$ ). This information would complement elemental abundance measurements of lighter and heavier  $n$ -capture species to get a more complete picture of the  $n$ -capture nucleosynthesis, constrain the conditions (e.g., temperature, neutron density, etc.) that are required to produce the  $r$ -process elements, and determine the actual  $r$ -process path by identifying the individual isotopes that participate in this process (see Cowan & Thielemann 2004 for further discussion). Extended discussion of the relationship between neutron densities in the "main" and "weak"  $r$ -processes and the isotopic abundance signatures in this mass range is provided in Kratz et al. (2007) and will not be repeated here. There is evidence that different mass regimes may be synthesized by different astrophysical processes in ad-

dition to the  $s$ - and  $r$ -processes, such as the light element primary process, or LEPP (Travaglio et al. 2004). While the LEPP would have the greatest effect on nucleosynthesis of lighter elements such as the Sr-Y-Zr group, knowledge of isotopic data for elements with very different  $Z$  would still be extremely informative.

This study has made use of the most current and complete laboratory atomic data to compute the isotope shifts and HFS patterns for Sm and Nd. While we are pleased that the available atomic data permits measurement of the isotopic fractions of these two species, complete sets of HFS constants and isotope shifts have not been measured for many lines that lie in the yellow-red regions of the spectrum. These transitions are generally weaker in stellar spectra, but the isotope shifts may be large enough nonetheless to permit reliable measurements of the isotopic fraction even with weak lines. We encourage such efforts from the atomic physics community in the future. We note that these lines may be significantly stronger in more metal-rich stars or those which exhibit enhanced abundances for  $s$ -process elements, such as Ba stars (e.g., Allen & Barbuy 2006a,b), where the blue lines we have used in our study are likely to be heavily blended with other atomic and molecular features; in these cases, lines in the yellow-red spectral regions may provide the only opportunity to establish the  $n$ -capture signatures at the isotopic level.

### 9.2. Individual Advantages and Disadvantages of Europium, Samarium, and Neodymium Isotopic Fractions

One advantage of using measurements of the Eu isotopic fraction as a nucleosynthesis probe is the wide HFS structure that can be measured with only moderately-high spectral resolution ( $R \sim 45\text{--}60,000$ ). In  $r$ -enriched stars, the Eu lines are strong enough to facilitate measurement of the isotopic fraction even at very low metallicities. But, as we have argued in § 6.1, it is unlikely that Eu isotopes can be measured with the precision to unambiguously distinguish  $s$ - and  $r$ -process nucleosynthesis using the lines in the near-UV and blue regions of the spectrum if indeed the Arlandini et al. (1999) predictions are correct.

Sm presents a different set of circumstances. The HFS of Sm is not nearly as wide as Eu, and the lines with the widest structure are also very weak (or undetectable) and sometimes blended in very metal-poor stars. Though we are forced to parametrize the  $s$ - and  $r$ -process nucleosynthetic predictions into some set of isotopes (e.g.,  $f_{\text{odd}}$  or  $f_{152+154}$ ) to facilitate distinguishing among seven isotopes simultaneously, the greater difference predicted between  $f_{152+154}^s$  and  $f_{152+154}^r$  allows one to cleanly distinguish these different nucleosynthetic signatures with reasonable measurement uncertainties. In addition, if Sm isotope fractions could be measured in a large sample of stars, it may be possible to observe the changing contributions of  $s$ - and  $r$ -process nucleosynthesis in stars over the history of the galaxy (cf. Figure 6 of Mashonkina & Zhao 2006, who performed a similar study using Ba isotopes). Therefore, while Sm lines that permit measurement of isotopic fractions may not be accessible in all metal-poor stars, we propose that in favorable cases Sm isotopes may give a clearer picture of the  $n$ -capture nucleosynthetic history than Eu isotopes can.

The Nd isotopic fraction is more difficult to measure reliably than the Sm isotopic fraction. The smaller isotope shifts of Nd translate directly into larger uncertainties in the measured isotopic fraction on any individual line. This necessitates that as many clean lines as possible be measured in order to reduce the uncertainties on the mean Nd isotopic fraction. Only then is it possible to unambiguously distinguish distinct chemical signatures in the Nd isotopes. Nd is produced more by the  $s$ -process than the  $r$ -process, though, so Nd lines may be easier to observe in stars with an  $s$ -process chemical signature than either Eu or Sm.

Of course these suggestions only apply to the examination of the nucleosynthetic history at the isotopic level. At the elemental level Eu should continue to serve as an excellent barometer of  $r$ -process nucleosynthesis, and Ba or La should continue to serve as barometers of  $s$ -process nucleosynthesis.

### 9.3. $s$ -process Yields from Models of Low-Metallicity Stars on the AGB

While the classical method of modeling the  $s$ -process is, by definition, model-independent, it has been shown to predict an overproduction of  $^{142}\text{Nd}$  relative to other isotopes of Nd and pure- $s$  nuclei, e.g., as determined from studies of the Murchison meteorite (Zinner et al. 1991; Guber et al. 1997). This isotope is only produced by the  $s$ -process and contains 82 neutrons, one of the magic neutron numbers, making this nucleus relatively more stable than other nuclei with similar mass numbers and thus violating the classical method's assumption of a smoothly-varying  $\sigma N_s$  curve. The complex stellar model of Arlandini et al. (1999) can avoid this difficulty near the magic neutron numbers.

Of the much theoretical and computational work that has been performed in recent years to better understand the structure and evolution of low-metallicity stars on the AGB, one goal has been to provide a complete set of chemical yields from H to Bi, at the termination of the  $s$ -process. The first such set of yields was presented by Cristallo (2006), for  $2M_{\odot}$  stars on the AGB with  $Z = 1.5 \times 10^{-2}$ ,  $1 \times 10^{-3}$ , and  $1 \times 10^{-4}$ . Similar models surely will follow, and the observational verification for these models will rely heavily on isotopic abundances as well as elemental abundances, particularly for magic neutron number nuclei such as  $^{142}\text{Nd}$ . The interpretation of  $n$ -capture nucleosynthetic signatures of the first generations of stars will depend heavily on the reliability of these models. As these models mature and are (hopefully) shown to be reliable predictors of  $s$ -process nucleosynthesis at low metallicity, they will provide insight into the structure and evolution of stars on the AGB that cannot be obtained from the classical ad hoc approach to understanding the  $s$ -process.

### 9.4. The Role of Future Studies of Neutron-Capture Isotopic Fractions

We suggest that the features which are strongly blended with the  $n$ -capture lines in our stars (in particular, Ti, V, Fe, and Ni) may be somewhat diminished in very metal-poor,  $n$ -capture enhanced stars. The requirements of high spectral resolution and high S/N to clearly discern  $n$ -capture isotopic fractions are currently

difficult to achieve for the numbers of such stars that have been detected by the HK Survey (Beers et al. 1985, 1992) and the Hamburg/ESO Survey (Wisotzki et al. 2000; Christlieb 2003), owing to the faintness of these stars. From a technical outlook, observations of this nature will become more feasible with high-resolution echelle spectrographs on the next generation of 20–30 m telescopes. Knowledge of the  $n$ -capture isotopic composition of these stars would complement the information gleaned from elemental abundances alone and further enhance our understanding of stellar nucleosynthesis and chemical evolution throughout the early history of our Galaxy.

## 10. CONCLUSIONS

We have successfully measured the isotopic fractions of Eu and Sm in HD 175305, and we have assessed the Nd isotopic fraction as well. We find that the Sm isotopic fraction is suggestive of an  $r$ -process origin. The Eu and Nd isotopic fractions are unable to distinguish between an  $r$ - or  $s$ -process origin. Along with measurements of elemental abundances of  $n$ -capture species, our Sm isotopic fraction reinforces the assertion that HD 175305 has been enriched by  $r$ -process nucleosynthesis. Both the elemental and isotopic abundance distributions in HD 175305 join the growing preponderance of evidence that supports the hypothesis of a universal  $r$ -process mechanism for elements with  $Z \geq 56$ .

We have measured the isotopic fraction of Sm in HD 196944, which suggests an  $s$ -process origin. The Nd isotopic fraction is unable to distinguish between the two processes. The Sm isotopic fraction complements previous elemental abundance measurements and observed radial velocity variations of this star to confirm that the enrichment pattern of HD 196944 is consistent with transfer of  $s$ -process material from a companion star in the AGB phase of stellar evolution.

We suggest that measurements of the Sm isotopic fraction will be more advantageous than measurements of the Eu isotopic fraction alone. The Sm isotopic fraction  $f_{152+154}$  permits a clearer distinction of pure- $s$ - and pure- $r$ -process content than Eu isotopic fractions can. There often are fewer blending features in the spectral regions where the useful Sm lines are located, and there are more Sm lines available for analysis. Nd lines may offer more opportunities to measure an isotopic fraction in  $s$ -process-enriched stars than either Eu or Sm, although it is extremely challenging to discern the Nd

isotopic fraction. We propose that measurements of isotopic fractions of multiple  $n$ -capture species in the same metal-poor star can allow direct quantification of the relative  $s$ - and  $r$ -process contributions to  $n$ -capture material, enable comparison of these contributions as a function of increasing nuclear mass number, test yields of low-metallicity stars on the AGB, and provide tests of  $s$ -process nucleosynthesis predictions. We have conducted one such test for  $^{151}\text{Eu}$  using Eu and Pb abundances collected from the literature, finding that the Arlandini et al. (1999) stellar model predictions are a better match than the classical method predictions for  $^{151}\text{Eu}$ , although this conclusion hinges on measurements of the Eu isotopic fraction in only two ( $r + s$ )-enriched stars.

Based on our results, we argue that the rare earth  $s$ - and  $r$ -process abundance patterns, which are observed in metal-poor stars at the elemental abundance level, are also present in the isotopic fractions. This implies that our understanding of  $n$ -capture nucleosynthesis is not wildly mistaken. This result has often been tacitly assumed in studies of nucleosynthesis and chemical abundance patterns in the Galactic halo, and we contend that increasing empirical evidence for multiple rare earth species now exists to support this hypothesis.

We are pleased to acknowledge the following individuals for their encouraging and helpful discussions: Carlos Allende Prieto, Jacob Bean, Anna Frebel, David Lambert, Martin Lundqvist, Rob Robinson, and Glenn Wahlgren. We thank the referee for providing a number of insightful comments on this manuscript. I. U. R. wishes to thank the McDonald Observatory staff for their hospitality and their dedication to the observatory, its visitors, and the West Texas community. This research has made use of the NASA Astrophysics Data System (ADS), NIST Atomic Spectra Database, Vienna Atomic Line Database (VALD; Kupka et al. 1999), Two Micron All-Sky Survey (2MASS), and SIMBAD databases. The reliability and accessibility of these online databases is greatly appreciated. Funding for this project has been generously provided by the U. S. National Science Foundation (grant AST 03-07279 to J. J. C., grant AST 05-06324 to J. E. L., and grants AST 03-07495 and AST 06-07708 to C. S.) and by the Sigma Xi *Grants-in-Aid-of-Research* program.

## APPENDIX

### COMMENTS ON INDIVIDUAL TRANSITIONS

Here we describe the individual characteristics of our lines of interest as well as blending features. Where possible, we have tried to incorporate the highest quality atomic data for these blending features, including  $\log(gf)$  values calculated from laser-induced fluorescence measurements of the radiative level lifetimes and branching fractions measured from Fourier transform spectrometry. We alert the reader that many of the studies published before the early 1980s used less precise methods, and we employ those values with some caution.

#### *Europium Lines*

The Eu II line at 4129Å is a clean, relatively unblended line in HD 175305; this spectral region was not observed in our other two stars. The only significant blend is a Fe I line at 4129.4611<sup>17</sup>Å in the far blue wing; the wavelength

<sup>17</sup> For wavelengths of blended features, we quote the number of digits to the right of the decimal point to the precision given in the reference and the precision used in our syntheses.

of this line was taken from Nave et al. (1994) and the  $\log(gf)$  value was taken from Fuhr & Wiese (2005), who scaled the value found by May et al. (1974). We note that these values are not critical to determining the isotopic fraction of Eu.

The Eu II line at 4205Å is strongly blended with CH (and, to a lesser extent, CN) features, two V II lines, and a Y II line. We adopt a CH linelist from the Kurucz database and a CN linelist from the Plez database<sup>18</sup>. Precise laboratory wavelengths and  $\log(gf)$  measurements are not available for the V II line at 4205.04Å; we adopt the V II 4205.084Å  $\log(gf)$  value from Biémont et al. (1989). A  $\log(gf)$  value for the Y II line at 4204.694Å can be calculated from the oscillator strength presented in Hannaford et al. (1982). Performing a synthesis of this region of the Solar spectrum using an interpolated empirical Holweger & Müller (1974) model atmosphere, we find rather poor agreement with the Kurucz et al. (1984) Solar flux spectrum, with the most significant discrepancies arising from the CH bands and the wavelength of the Y II line. One would hope that in a very metal-poor star with sub-solar C abundance (HD 122563) these effects would be greatly diminished; the situation is much less hopeful for a C-enhanced star (HD 196944). Yet given the extent and severity of the blends of this Eu line, as well as its weakness in HD 122563, we are reluctant to trust any of the isotope fractions derived from this line. This is unfortunate because only this Eu line is strong enough to permit measurement of the elemental abundance in our observed spectra in HD 122563 and HD 196944.

The Eu II line at 4435Å is strongly blended with a Ca I line at 4435.67Å and mildly blended with a Ni I line at 4435.33Å. In HD 122563 and HD 196944, this Eu line is only a small sliver on the blue wing of the Ca line, and therefore no reasonable assessment of the elemental abundance or isotopic fraction can be made. In HD 175305 the Ca line is saturated, and we cannot produce a satisfactory fit to the blended profile no matter what  $\log(gf)$  value we adopt for this line. We adjust the  $\log(gf)$  value of the Ni line to match the Solar spectrum, yet an additional adjustment of +0.65 dex to the Solar  $\log(gf)$  value is necessary to bring this line into rational agreement with our observed spectrum. Even then we are not satisfied with the fit of the blue wing of the Eu line. Consequently, because such a small region of the spectrum covered by the Eu line remains unblended, we also disregard this line in our measurement of the isotopic fraction.

#### *Samarium Lines*

The Sm II line at 4424.34Å is relatively strong and is blended only slightly with a Cr I line at 4424.28Å. An unpublished  $\log(gf)$  value for this line,  $-0.63$ , was measured by Sobek et al. (2007). We measure Sm isotopic fractions from this line in HD 175305 and HD 196944; the line is too weak to measure well in HD 122563.

The Sm II line at 4467.34Å is also relatively strong and blended slightly with a weak Fe I line at 4467.43Å and an unidentified (in, e.g., the Moore et al. 1966 atlas) line at 4467.21Å. No experimental  $\log(gf)$  value is available for the Fe line, but we use an inverted Solar analysis to derive a  $\log(gf)$  of  $-2.92$  for this line. The unidentified feature can be reasonably modeled as an Fe line. The isotope shifts of this line are almost negligible and the HFS is also small, but Ekeland & Hauge (1975) used it in their analysis of the Sm isotopic fraction in the Sun. This line is not covered in any of our stellar spectra, but we do use it to revisit the Sm isotopic fraction in the Solar photosphere.

The Sm II 4591.81Å line lies near the edge of the blue wing of a strong Cr I line at 4592.05Å that is easily accounted for in the synthesis. Of greater concern, however, is an apparently unidentified blend at 4591.73Å in HD 175305. We do not measure an isotopic fraction from this line but suggest that it might be useful in future studies. In HD 122563 this line just falls off an echelle order, and in HD 196944 this line is too weak to observe.

The Sm II 4593.53Å line is affected by a very weak Fe I line at 4593.53Å, whose  $\log(gf)$  value is given by Fuhr & Wiese (2005), which has been scaled from May et al. (1974). We also notice a small, unidentified blend in the blue wing of this line at 4593.42Å; a close examination of Lundqvist et al. (2007)'s spectrum of CS 31082-001 in Figure 5 shows a similar feature. This Sm line is too weak to be observed in HD 122563, is observed but is too weak to assess the isotopic fraction in HD 196944, and, regrettably, in HD 175305 this line fell on a piece of the CCD where we encountered unrecoverable flat-fielding errors during the reduction process.

The Sm II 4595.28Å line is severely blended with a strong Fe I line at 4595.3591Å. The  $\log(gf)$  value for this Fe line can be computed from the data in O'Brian et al. (1991), but we are hesitant to believe any Sm abundances derived from this line in any of our stars.

The Sm II line at 4604.17Å is promising. A Fe I line at 4603.949Å affects only the bluest wing of this line, and a weak Fe I line blends with it at 4604.24Å; a  $\log(gf)$  value is available for the latter of these two Fe lines in Gurtovenko & Kostik (1981) and the  $\log(gf)$  for the former is derived from an inverted Solar analysis ( $-3.15$ ), which provides a far better fit than the  $\log(gf)$  rated an "E" in Fuhr & Wiese (2005). We measure an isotopic fraction for this line in HD 175305, but the line is too weak in the other two stars.

The Sm II 4693.63Å line is blended with a Ti I line at 4693.67Å. Using our Ti I abundance and the  $\log(gf)$  value for this line from Kühne et al. (1978), we cannot produce a satisfactory fit for the Sm line. An additional unidentified blend occurs at 4693.75Å in our spectrum of HD 175305. Our spectra of HD 122563 and HD 196944 do not cover this region. We do not make a measurement of the elemental abundance or isotopic fraction of Sm from this line in HD 175305, but we suggest that this line could be a candidate for future Sm isotopic analyses.

Lundqvist et al. (2007) note that the Sm II line at 4715.27Å is blended with a Ti I line at 4715.230Å. A  $\log(gf)$  value is available in Kühne et al. (1978). This line was not covered in any of our spectra, but isotopic analysis of this

<sup>18</sup> Available online: <ftp://saphir.dstu.univ-montp2.fr/GRAAL/plez/CNdata>

Sm line may be possible.

The Sm II line at 4719.84Å is covered in all three of our spectra, but is only strong enough to measure in HD 175305 and HD 196944. Full sets of hyperfine A and B constants are not available for this line, so we compute the profile using only the isotope shifts measured by Lundqvist et al. (2007). This line is blended with a weak La II line at 4719.92Å; this La line was not included in the analysis of Lawler et al. (2001a). While the Sm line is much stronger than the La line in both of our spectra, the uncertainty in the La  $\log(gf)$  value and the lack of HFS structure information for the Sm line lead us to disregard this line in our isotopic analysis.

The Sm II line at 5052.75Å is not covered in any of our spectra. Full sets of hyperfine A and B constants are not available for this line, either, but we compute a synthesis using the isotope shifts only. This line is blended with a Ti I line at 5052.87Å and a Fe I line at 5052.9814Å. A  $\log(gf)$  value is listed for the Ti line in the catalog of Savanov (1990), and a wavelength for the Fe line is given in Nave et al. (1994). We suggest that these blends may be able to be accounted for even without precise atomic data, and the isotope shifts alone could provide some indication of the Sm isotopic fraction in metal-poor stars, but measurement of an exact isotopic fraction is probably unwarranted here.

The weak Sm II line at 5069.47Å is blended with a weak Fe I line at 5069.4233Å, which is blended with a weak Ti I line at 5069.35Å. The wavelength for this Fe line is listed in Nave et al. (1994), but we cannot find an experimental  $\log(gf)$  value for this line, and the Ti blend prevents us from using an inverted Solar analysis to derive a  $\log(gf)$  value for either line. We observe the Sm line in our spectra of HD 122563 and HD 196944; however, in both cases the Sm line is weak and the observed spectrum is littered with small, undocumented blends in addition to the Fe line noted here. We recommend that any attempts to use this line for Sm isotopic analysis proceed with great caution.

The Sm II line at 5103.09Å is weak and lies on the red edge of a strong Ni I line at 5102.964Å. A  $\log(gf)$  value for the Ni line is given in Doerr & Kock (1985), and we have set the wavelength of this line from analysis of the Solar spectrum. Full sets of hyperfine A and B constants are not available for this line, yet we compute a synthetic spectrum using only the isotope shifts. We can detect the Sm line in HD 175305, but it is so overwhelmed by the Ni line that we cannot trust even our derived elemental abundance. This Sm line is too weak to detect in HD 122563 and HD 196944.

Our redmost Sm II line lies at 5104.48Å. It is blended by a Fe I line at 5104.4375Å. Nave et al. (1994) quote a precise wavelength for this Fe line, and its  $\log(gf)$  value is listed in Fuhr & Wiese (2005), who scaled May et al. (1974)'s value. When we synthesize this line in HD 175305, we are forced to enhance the Sm abundance by more than a factor of 2. We have re-evaluated the  $\log(gf)$  value of the Fe blend by comparing with the Solar spectrum, and find that we can reasonably only increase Fuhr & Wiese (2005)'s  $\log(gf)$  value by  $\approx 0.2$  dex, which does little to provide a better match between our observed and synthetic spectra. In addition, there is a significant unidentified blend at 5104.59Å in the red wing of our Sm line. While it is clear that the Sm line is broadened by HFS and isotopic shifts, we unfortunately are unable to measure an isotopic fraction. This Sm line is too weak to detect in HD 122563 and is not covered in our spectrum of HD 196944.

#### *Neodymium Lines*

The Nd II line at 4177.32Å is relatively strong, and only its far red wing is blended with a strong Y II and Fe I blend. A  $\log(gf)$  value can be calculated for the Y II line at 4177.536Å from the  $f$ -value in Hannaford et al. (1982), and a  $\log(gf)$  value for the Fe I line at 4177.5935Å is given in O'Brian et al. (1991). This blend is easily accounted for and has little effect on the derived Nd isotopic fraction. This Nd line was not covered in our spectra of HD 122563 and HD 196944, but we measure an isotopic fraction from this line in HD 175305.

The Nd II line at 4232.38Å has two identified blends. The Hf II line at 4232.386Å lies coincident with our Nd line; a  $\log(gf)$  value for this line was measured by Lundqvist et al. (2006). A V I line at 4232.46Å also blends with our Nd line, and a  $\log(gf)$  value is provided by Martin et al. (1988) in the NIST database. The uncertainties in the abundances and transition probabilities of these two lines, as well as their severity of blending with our Nd feature, lead us to disregard this line in our spectrum of HD 175305. This line was not covered in our spectra of HD 122563 and HD 196944. The isotope shifts of this Nd line are noticeable, though, so we report the hyperfine patterns for this line nonetheless.

The Nd II line at 4314.51Å lies in a region where continuum placement is difficult due to the presence of the CH G-band. We have not attempted to measure the Nd isotopic fraction from this line in any of our stars, although the Nd line is visible in HD 175305 and HD 196944. The isotope shifts of this line are rather large ( $\sim 0.035$ Å), so we report the hyperfine patterns for this line, in hopes that the Nd isotopic fraction could be discerned from this line in a favorable star. Den Hartog et al. (2003) did not measure a  $\log(gf)$  value for this line, but we derive  $\log(gf) = -0.22$  from an inverted Solar analysis, assuming  $\log \varepsilon(\text{Nd})_{\odot} = 1.50$ .

The Nd II line at 4358.16Å is relatively strong and unblended in HD 175305, and we use it to measure an isotopic fraction. This line was not covered in our spectra of HD 122563 and HD 196944.

The Nd II line at 4446.38Å has the largest isotope shifts of any of the Nd transitions for which we report an isotopic fraction. In HD 175305, this line is blended only with a weak Gd II line at 4446.502Å in the red wing, and Den Hartog et al. (2006) provide a  $\log(gf)$  value for this line. In HD 196944, some unidentified blends are observed in both the red and blue wings of this line, but it does not appear that these blends affect our measurement of the isotope fraction. We measure an isotopic fraction from this line in each of these two stars. This line is observed in our high-S/N spectrum of HD 122563, but it has a continuum depth of only  $\sim 1.5\%$ , and we cannot measure an isotopic fraction from this line.

The Nd II line at 4567.61Å has a depth of only 4% in HD 175305, and an isotopic fraction can only marginally be deduced from this line. We identify no blending features, although our observed spectrum clearly shows some weaker blends in the wings of this line. This line was not covered in our observed spectra of HD 122563 and HD 196944.

## HYPERFINE COMPONENT DATA FOR SAMARIUM

We present hyperfine and isotopic components for the 13 lines of Sm II described in § A.2 in Table 4. Hyperfine A (magnetic dipole) and B (electric quadrupole) constants, which govern the relative positions of the hyperfine components, along with isotope shifts, were taken first from Masterman et al. (2003) if available. Constants for additional levels were taken from Dörschel et al. (1981), Young et al. (1987), and Villemoes et al. (1995). We give preference to the hyperfine constants and isotope shifts determined from radio frequency measurements or with a single-frequency laser, as in Masterman et al. (2003) and Beiersdorf et al. (1995), supplemented with isotope shifts measured from FTS spectra in Lundqvist et al. (2007) for lines not covered in earlier studies.

The relative strengths are calculated from the LS (Russell-Saunders) angular momentum coupling formulae (e.g., Condon & Shortley 1953, p. 238), where we have replaced the orbital angular momentum quantum number ( $L$ ) by the total electronic angular momentum ( $J$ ), the electron spin ( $S$ ) by the nuclear spin ( $I$ ), and the total electronic angular momentum ( $J$ ) by the total atomic angular momentum ( $F$ ). Thus,  $F = I + J$ , and the energy of the  $J$  level is split into a number of sublevels given by  $F$ , which runs from  $|I - J|$  to  $I + J$ . The energy spacing between each component is proportional to  $F$ . The nucleus may also have an electric quadrupole moment, which produces an additional shift (but not splitting) in the energy levels. The strongest relative components are those for which  $\Delta F = \Delta J$ . We normalize the strengths for each line such that they sum to one. Absolute transition wavenumbers are from Lundqvist et al. (2007) if the lines were included in their study, otherwise they are computed using the energy levels tabulated by Martin et al. (1978). The center-of-gravity transition wavenumbers and air wavelengths are given in the first two columns, respectively. Component wavenumbers are converted to air wavelengths according to the formula given by Edlén (1953).

## HYPERFINE COMPONENT DATA FOR NEODYMIUM

We present hyperfine and isotopic components for the 6 lines of Nd II described in § A.3 in Table 5. Hyperfine A and B constants and isotope shifts were taken from Rosner et al. (2005). All calculations were performed analogously to the Sm case. Center-of-gravity transition wavenumbers for the lines of interest were taken from FTS measurements by Blaise et al. (1984).

## REFERENCES

- Allen, D. M., & Barbuy, B. 2006, *A&A*, 454, 895  
 Allen, D. M., & Barbuy, B. 2006, *A&A*, 454, 917  
 Alonso, A., Arribas, S., & Martínez-Roger, C. 1996, *A&A*, 313, 873  
 Alonso, A., Arribas, S., & Martínez-Roger, C. 1999, *A&AS*, 140, 261  
 Anders, E., & Grevesse, N. 1989, *Geochim. Cosmochim. Acta*, 53, 197  
 Aoki, W., et al. 2001, *ApJ*, 561, 346  
 Aoki, W., Ryan, S. G., Norris, J. E., Beers, T. C., Ando, H., & Tsangarides, S. 2002, *ApJ*, 580, 1149  
 Aoki, W., Honda, S., Beers, T. C., & Sneden, C. 2003a, *ApJ*, 586, 506  
 Aoki, W., et al. 2003b, *ApJ*, 592, L67  
 Aoki, W., et al. 2005, *ApJ*, 632, 611  
 Aoki, W., Bisterzo, S., Gallino, R., Beers, T. C., Norris, J. E., Ryan, S. G., & Tsangarides, S. 2006, *ApJ*, 650, L127  
 Aoki, W., et al. 2007, *ApJ*, 660, 747  
 Arlandini, C., Käppeler, F., Wisshak, K., Gallino, R., Lugaro, M., Busso, M., & Straniero, O. 1999, *ApJ*, 525, 886  
 Asplund, M., Nordlund, A., Trampedach, R., Allende Prieto, C., & Stein, R. F., 2000, *A&A*, 359, 729  
 Asplund, M. 2004, *Mem. Soc. Astron. Italiana*, 75, 300  
 Asplund, M., Lambert, D. L., Nissen, P. E., Primas, F., & Smith, V. V. 2006, *ApJ*, 644, 229  
 Barbuy, B., et al. 2003, *ApJ*, 588, 1072  
 Barbuy, B., Spite, M., Spite, F., Hill, V., Cayrel, R., Plez, B., & Petitjean, P. 2005, *A&A*, 429, 1031  
 Barklem, P. S., et al. 2005, *A&A*, 439, 129  
 Beers, T. C., Preston, G. W., & Shectman, S. A. 1985, *AJ*, 90, 2089  
 Beers, T. C., Preston, G. W., & Shectman, S. A. 1992, *AJ*, 103, 1987  
 Beers, T. C., & Christlieb, N. 2005, *ARA&A*, 43, 531  
 Beiersdorf, S., Heddrich, W., Kesper, K., Hühnermann, H., Möller, W., & Wagner, H. 1995, *J. Phys. G: Nucl. Part. Phys.* 21, 215  
 Biémont, E., Grevesse, N., Faires, L. M., Marsden, G., & Lawler, J. E. 1989, *A&A*, 209, 391  
 Biémont, E., Garnir, H. P., Palmeri, P., Li, Z. S., & Svanberg, S. 2000, *MNRAS*, 312, 116  
 Blaise, J., Wyart, J. F., Djerad, M. T., & Ahmed, Z. B. 1984, *Phys. Scr.*, 29, 119  
 Bond, H. E. 1980, *ApJS*, 44, 517  
 Brandt, H.-W., Meißner, E., & Steudel, A. 1979, *Z. Physik A*, 291, 97  
 Brown, J. A., Wallerstein, G., Cunha, K., & Smith, V. V. 1991, *A&A*, 249, L13  
 Burris, D. L., Pilachowski, C. A., Armandroff, T. E., Sneden, C., Cowan, J. J., & Roe, H. 2000, *ApJ*, 544, 302  
 Busso, M., Gallino, R., & Wasserburg, G. J. 1999, *ARA&A*, 37, 239  
 Carney, B. W., Latham, D. W., Stefanik, R. P., Laird, J. B., & Morse, J. A. 2003, *AJ*, 125, 293  
 Cayrel, R., et al. 2007, *A&A*, 473, L37  
 Cescutti, G., François, P., Matteucci, F., Cayrel, R., & Spite, M. 2006, *A&A*, 448, 557  
 Christlieb, N. 2003, *Reviews in Modern Astronomy*, 16, 191  
 Clayton, D. D., Fowler, W. A., Hull, T. E., & Zimmermann, B. A. 1961, *Ann. Phys.*, 12, 331  
 Cohen, J. G., Christlieb, N., Qian, Y.-Z., & Wasserburg, G. J. 2003, *ApJ*, 588, 1082  
 Cohen, J. G., et al. 2006, *AJ*, 132, 137  
 Condon, E. U., & Shortley, G. H. 1953, *The Theory of Atomic Spectra* (Cambridge: Cambridge Univ. Press), 238  
 Cowan, J. J., Pfeiffer, B., Kratz, K.-L., Thielemann, F.-K., Sneden, C., Burles, S., Tytler, D., & Beers, T. C. 1999, *ApJ*, 521, 194  
 Cowan, J. J., et al. 2002, *ApJ*, 572, 861  
 Cowan, J. J., & Thielemann, F.-K. 2004, *Physics Today*, 57, 47  
 Cowan, J. J., et al. 2005, *ApJ*, 627, 238  
 Cowan, J. J., Lawler, J. E., Sneden, C., Den Hartog, E. A., & Collier, J. 2006, in *Proc. NASA LAW*, ed. V. Kwong, (Washington: NASA), 82

- Cowan, J. J., & Sneden, C. 2006, *Nature*, 440, 1151
- Cowley, C. R., & Corliss, C. H. 1983, *MNRAS*, 203, 651
- Cowley, C. R., & Frey, M. 1989, *ApJ*, 346, 1030
- Cristallo, S. 2006, Ph.D. Thesis, Osservatorio Astronomico di Collurania
- Den Hartog, E. A., Lawler, J. E., Sneden, C., & Cowan, J. J. 2003, *ApJS*, 148, 543
- Den Hartog, E. A., Lawler, J. E., Sneden, C., & Cowan, J. J. 2006, *ApJS*, 167, 292
- Doerr, A., & Kock, M. 1985, *J. Quant. Spec. Radiat. Transf.*, 33, 307
- Dörschel, K., Hühnermann, H., Knobl, E., Meier, Th., & Wagner, H. 1981, *Z. Phys. A – Atoms and Nuclei*, 302, 359
- Dravins, D., Lindgren, L., & Nordlund, A. 1981, *A&A*, 96, 345
- Dravins, D., Larsson, B., & Nordlund, A. 1986, *A&A*, 158, 83
- Dravins, D. 1987, *A&A*, 172, 211
- Edvardsson, B., Andersen, J., Gustafsson, B., Lambert, D. L., Nissen, P. E., & Tomkin, J. 1993, *A&A*, 275, 101
- Edlén, B. 1953, *J. Opt. Soc. Am.*, 43, 339
- Ekeland, A., & Hauge, Ø. 1975, *Sol. Phys.*, 42, 17
- Fitzpatrick, M. J., & Sneden, C. 1987, *BAAS*, 19, 1129
- François, P., et al. 2007, *A&A*, doi:10.1051/0004-6361
- Frebel, A., Christlieb, N., Norris, J. E., Thom, C., Beers, T. C., & Rhee, J. 2007, *ApJ*, 660, L117
- Fuhr, J. R., & Wiese, W. L. 2005, *J. Phys. Chem. Ref. Data*, 35, 1669
- Fulbright, J. P. 2000, *AJ*, 120, 1841
- Fulbright, J. P. 2002, *AJ*, 123, 404
- Gallino, R., Arlandini, C., Busso, M., Lugaro, M., Travaglio, C., Straniero, O., Chieffi, A., & Limongi, M. 1998, *ApJ*, 497, 388
- Gallino, R., Delaude, D., Husti, L., Cristallo, S., Straniero, O., & Ryan, S. 2005, *Nuclear Physics A*, 758, 485
- Gratton, R. G., & Sneden, C. 1994, *A&A*, 287, 927
- Gray, D. F. 2005, *The Observation and Analysis of Stellar Photospheres*, 3rd Edition. Cambridge, UK: Cambridge University Press
- Grvesse, N., & Sauval, A. J. 2002, *Adv. Space Res.*, 30, 3
- Guber, K. H., Spencer, R. R., Koehler, P. E., & Winters, R. R. 1997, *Phys. Rev. Lett.*, 78, 2704
- Gurtovenko, E. A., & Kostik, R. I. 1981, *A&AS*, 46, 239
- Hannaford, P., Lowe, R. M., Grvesse, N., Biemont, E., & Whaling, W. 1982, *ApJ*, 261, 736
- Hauge, Ø. 1970, *Sol. Phys.*, 11, 17
- Hauge, Ø. 1972, *Sol. Phys.*, 27, 286
- Hill, V., et al. 2002, *A&A*, 387, 560
- Holweger, H., & Müller, E. A. 1974, *Sol. Phys.*, 39, 19
- Honda, S., et al. 2004a, *ApJS*, 152, 113
- Honda, S., Aoki, W., Kajino, T., Ando, H., Beers, T. C., Izumiura, H., Sadakane, K., & Takada-Hidai, M. 2004b, *ApJ*, 607, 474
- Honda, S., Aoki, W., Ishimaru, Y., Wanajo, S., & Ryan, S. G. 2006, *ApJ*, 643, 1180
- Honda, S., Aoki, W., Ishimaru, Y., & Wanajo, S. 2007, *ApJ*, 666, 1189
- Ivans, I. I., Sneden, C., Gallino, R., Cowan, J. J., & Preston, G. W. 2005, *ApJ*, 627, L145
- Ivans, I. I., Simmerer, J., Sneden, C., Lawler, J. E., Cowan, J. J., Gallino, R., & Bisterzo, S. 2006, *ApJ*, 645, 613
- Johnson, J. A. 2002, *ApJS*, 139, 219
- Johnson, J. A., & Bolte, M. 2002, *ApJ*, 579, 616
- Johnson, J. A., & Bolte, M. 2002, *ApJ*, 579, L87
- Johnson, J. A., Herwig, F., Beers, T. C., & Christlieb, N. 2007, *ApJ*, 658, 1203
- Jonsell, K., Edvardsson, B., Gustafsson, B., Magain, P., Nissen, P. E., & Asplund, M. 2005, *A&A*, 440, 321
- Jonsell, K., Barklem, P. S., Gustafsson, B., Christlieb, N., Hill, V., Beers, T. C., & Holmberg, J. 2006, *A&A*, 451, 651
- Käppeler, F., Beer, H., & Wisshak, K. 1989, *Rep. Prog. Phys.*, 52, 945
- Klose, J. Z., Fuhr, J. R., & Wiese, W. L. 2002, *J. Phys. Chem. Ref. Data*, 31, 217
- Kratz, K.-L., Farouqi, K., Pfeiffer, B., Truran, J. W., Sneden, C., & Cowan, J. J. 2007, *ApJ*, 662, 39
- Kühne, M., Danzmann, K., & Kock, M. 1978, *A&A*, 64, 111
- Kupka, F., Piskunov, N., Ryabchikova, T. A., Stempels, H. C., & Weiss, W. W. 1999, *A&AS*, 138, 119
- Kurucz, R. L., Rurenid, I., Brault, J., & Testerman, L. 1984, *Solar Flux Atlas from 296 to 1300 nm*, National Solar Observatory Atlas No. 1 (Harvard University)
- Kurucz, R. L. 1993, *Kurucz CD-ROM 13, ATLAS9 Stellar Atmosphere Programs and 2 km/s Grid* (Cambridge: SAO)
- Kurucz, R. L., & Bell, B. 1995, *CD-ROM*, Cambridge, MA: Smithsonian Astrophysical Observatory
- Lambert, D. L., & Sneden, C. 1977, *ApJ*, 215, 597
- Lambert, D. L., & Allende Prieto, C. 2002, *MNRAS*, 335, 325
- Lawler, J. E., Bonvallet, G., & Sneden, C. 2001a, *ApJ*, 556, 452
- Lawler, J. E., Wickliffe, M. E., den Hartog, E. A., & Sneden, C. 2001b, *ApJ*, 563, 1075
- Lawler, J. E., Den Hartog, E. A., Sneden, C., & Cowan, J. J. 2006, *ApJS*, 162, 227
- Lawler, J. E., Den Hartog, E. A., Labby, Z. E., Sneden, C., Cowan, J. J., & Ivans, I. I. 2007, *ApJS*, 169, 120
- Learner, R. C. M., & Thorne, A. P. 1988, *J. Opt. Soc. Am. B*, 5, 2045
- Lodders, K. 2003, *ApJ*, 591, 1220
- Lucatello, S., Tsangarides, S., Beers, T. C., Carretta, E., Gratton, R. G., & Ryan, S. G. 2005, *ApJ*, 625, 825
- Lundqvist, M., Nilsson, H., Wahlgren, G. M., Lundberg, H., Xu, H. L., Jang, Z.-K., & Leckrone, D. S. 2006, *A&A*, 450, 407
- Lundqvist, M., Wahlgren, G. M., & Hill, V. 2007, *A&A*, 463, 693
- Magain, P., & Zhao, G. 1993a, *Origin and evolution of the elements: proceedings of a symposium in honor of H. Reeves, held in Paris, June 22-25, 1992*. Edited by Prantzos, N., Vangioni-Flam, E., & Casse, M. Published by Cambridge University Press, Cambridge, England, 1993, 480
- Magain, P., & Zhao, G. 1993b, *A&A*, 268, L27
- Magain, P. 1995, *A&A*, 297, 686
- Martin, W. C., Zalubas, R., & Hagan, L. 1978, *NSRDS-NBS*, Washington: National Bureau of Standards, U.S. Department of Commerce, —c1978, p. 174
- Martin, G. A., Fuhr, J. R., & Wiese, W. L. 1988, *J. Phys. Chem. Ref. Data*, 17, Suppl. 3
- Mashonkina, L., Gehren, T., & Bikmaev, I. 1999, *A&A*, 343, 519
- Mashonkina, L., Gehren, T., Travaglio, C., & Borkova, T. 2003, *A&A*, 397, 275
- Mashonkina, L. I., Kamaeva, L. A., Samotoev, V. A., & Sakhbullin, N. A. 2004, *Astronomy Reports*, 48, 185
- Mashonkina, L., & Zhao, G. 2006, *A&A*, 456, 313
- Masseron, T., et al. 2006, *A&A*, 455, 1059
- Masterman, D., Rosner, S. D., Scholl, T. J., Sharikova, A., & Holt, R. A. 2003, *Can. J. Phys.*, 81, 1389
- May, M., Richter, J., & Wichelmann, J. 1974, *A&AS*, 18, 405
- McWilliam, A. 1998, *AJ*, 115, 1640
- Meyer, B. S., & Clayton, D. D. 2000, *Space Sci. Rev.*, 92, 133
- Moore, C. E., Minnaert, M. G. J., & Houtgast, J. 1966, *National Bureau of Standards Monograph*, Washington: US Government Printing Office (USGPO), 1966,
- Nave, G., Johansson, S., Learner, R. C. M., Thorne, A. P., & Brault, J. W. 1994, *ApJS*, 94, 221
- Nordström, B., et al. 2004, *A&A*, 418, 989
- Norlén, G. 1973, *Phys. Scr*, 8, 249
- O'Brian, T. R., Wickliffe, M. E., Lawler, J. E., Whaling, W., & Brault, J. W. 1991, *J. Opt. Soc. Am. B*, 8, 1185
- Palmeri, P., Quinet, P., Wyart, J.-F., & Biémont, E. 2000, *Phys. Scr*, 61, 323
- Pickering, J. C., Thorne, A. P., & Perez, R. 2001, *ApJS*, 132, 403
- Pickering, J. C., Thorne, A. P., & Perez, R. 2002, *ApJS*, 138, 247
- Plez, B., et al. 2004, *A&A*, 428, L9
- Press, W. H., Teukolsky, S. A., Vetterling, W. T., & Flannery, B. P. 1992, *Numerical Recipes in FORTRAN: The Art of Scientific Computing*, (2nd ed.; Cambridge: University Press), 655
- Preston, G. W., Thompson, I. B., Sneden, C., Stachowski, G., & Shtetman, S. A. 2006, *AJ*, 132, 1714
- Qian, Y.-Z., & Wasserburg, G. J. 2000, *Phys. Rep.*, 333, 77
- Ramírez, I., & Meléndez, J. 2005, *ApJ*, 626, 465
- Rao, P. M., Ahmad, S. A., Venugopalan, A., & Saksena, G. D., 1990, *Z. Phys. D – Atoms, Molecules, and Clusters*, 15, 211
- Rosman, K. J. R., & Taylor, P. D. P. 1998, *Pure Appl. Chem.*, 70, 217
- Rosner, S. D., Masterman, D., Scholl, T. J., & Holt, R. A. 2005, *Can. J. Phys.*, 83, 841

- Savanov, I. S. 1990, 3rd International Collogium of the Royal Netherlands Academy of Arts and Sciences, 165
- Seeger, P. A., Fowler, W. A., & Clayton, D. D. 1965, *ApJS*, 11, 121
- Short, C. I., & Hauschildt, P. H. 2006, *ApJ*, 641, 494
- Simmerer, J., Sneden, C., Cowan, J. J., Collier, J., Woolf, V. M., & Lawler, J. E. 2004, *ApJ*, 617, 1091
- Skrutskie, M. F., et al. 2006, *AJ*, 131, 1163
- Smith, V. V., Vargas-Ferro, O., Lambert, D. L., & Olgin, J. G. 2001, *AJ*, 121, 453
- Sneden, C. A. 1973, Ph.D. Thesis, Univ. Texas at Austin
- Sneden, C., Kraft, R. P., Prosser, C. F., & Langer, G. E. 1991, *AJ*, 102, 2001
- Sneden, C., Kraft, R. P., Langer, G. E., Prosser, C. F., & Shetrone, M. D. 1994, *AJ*, 107, 1773
- Sneden, C., Cowan, J. J., Lawler, J. E., Burles, S., Beers, T. C., & Fuller, G. M. 2002, *ApJ*, 566, L25
- Sneden, C., et al. 2003, *ApJ*, 591, 936
- Sobeck, J. S., Lawler, J. E., & Sneden, C. 2007, *ApJ*, 667, 1267
- Spite, M., & Spite, F. 1978, *A&A*, 67, 23
- Straniero, O., Gallino, R., & Cristallo, S. 2006, *Nuclear Physics A*, 777, 311
- Travaglio, C., Galli, D., Gallino, R., Busso, M., Ferrini, F., & Straniero, O. 1999, *ApJ*, 521, 691
- Travaglio, C., Galli, D., & Burkert, A. 2001, *ApJ*, 547, 217
- Travaglio, C., Gallino, R., Arnone, E., Cowan, J., Jordan, F., & Sneden, C. 2004, *ApJ*, 601, 864
- Tull, R. G., MacQueen, P. J., Sneden, C., & Lambert, D. L. 1995, *PASP*, 107, 251
- Van Eck, S., Goriely, S., Jorissen, A., & Plez, B. 2001, *Nature*, 412, 793
- Van Eck, S., Goriely, S., Jorissen, A., & Plez, B. 2003, *A&A*, 404, 291
- Villemoes, P., Wang, M., Arnesen, A., Weiler, C., & Wännström, A. 1995, *Phys. Rev. A*, 51, 2838
- Wallerstein, G., Pilachowski, C., Gerend, D., Baird, S., & Canterna, R. 1979, *MNRAS*, 186, 691
- Wanajo, S., & Ishimaru, Y. 2006, *Nucl. Phys. A*, 777, 676
- Wasserburg, G. J., Busso, M., & Gallino, R. 1996, *ApJ*, 466, L109
- Wasserburg, G. J., & Qian, Y.-Z. 2000, *ApJ*, 529, L21
- Whaling, W., Anderson, W. H. C., Carle, M. T., Brault, J. W., & Zaren, H. A. 2002, *J. Res. Natl. Inst. Stand. Technol.*, 107, 149
- Wickliffe, M. E., Lawler, J. E., & Nave, G. 2000, *J. Quant. Spec. Radiat. Transf.*, 66, 363
- Winckler, N., Dababneh, S., Heil, M., Käppeler, F., Gallino, R., & Pignatari, M. 2006, *ApJ*, 647, 685
- Wisotzki, L., Christlieb, N., Bade, N., Beckmann, V., Köhler, T., Vanelle, C., & Reimers, D. 2000, *A&A*, 358, 77
- Wujec, T., & Weniger, S. 1981, *J. Quant. Spec. Radiat. Transf.*, 25, 167
- Yong, D., Aoki, W., Lambert, D. L., & Paulson, D. B. 2006, *ApJ*, 639, 918
- Young, L., Childs, W. J., Berry, H. G., Kurtz, C., & Dinneen, T. 1987, *Phys. Rev. A*, 36, 2148
- Začs, L., Nissen, P. E., & Schuster, W. J. 1998, *A&A*, 337, 216
- Zinner, E., Amari, S., & Lewis, R. S. 1991, *ApJ*, 382, L47

TABLE 1  
COMPARISON OF MODEL ATMOSPHERE PARAMETERS

Reference	$T_{\text{eff}}$ (K)	$\log(g)$	[M/H]	[Fe/H] <sup>a</sup>	$v_{\text{micro}}$ (km s <sup>-1</sup> )	$v_{\text{macro}}$ (km s <sup>-1</sup> )
HD 122563						
This study	4430	0.55	-2.63	-2.83	2.4	4.4
Fulbright (2000)	4425	0.6	...	-2.6	2.75	...
Johnson (2002)	4450	0.50	-2.65	-2.75	2.30	...
Honda et al. (2004b)	4570	1.1	...	-2.77	2.2	...
Simmerer et al. (2004)	4572	1.36	...	-2.72	2.90	...
HD 175305						
This study	4870	2.15	-1.40	-1.60	1.2	4.6
Fulbright (2000)	4575	2.4	...	-1.30	1.4	...
Burris et al. (2000)	5100	2.50	-1.50	-1.40	1.40	...
Cowan et al. (2005)	5040	2.85	...	-1.48	2.00	...
HD 196944						
This study	5170	1.80	-2.26	-2.46	1.7	6.8
Začs et al. (1998)	5250	1.7	-2.0	-2.45	1.9	...
Aoki et al. (2002)	5250	1.8	...	-2.25	1.7	...

<sup>a</sup> [Fe I/H] is listed here. We find [Fe II/H] = -2.79 for HD 122563, [Fe II/H] = -1.62 for HD 175305, and [Fe II/H] = -2.43 for HD 196944.

TABLE 2  
ISOTOPE MIXES FOR PURE *s*- AND *r*-PROCESS MATERIAL AND MEASURED ISOTOPIC FRACTIONS

Species	stellar model <sup>a</sup>		classical method <sup>b</sup>		Solar System <sup>c</sup>	HD 175305	HD 196944
	<i>s</i> -only	<i>r</i> -only	<i>s</i> -only	<i>r</i> -only			
Ba: $f_{\text{odd}} =$	0.11	0.46	0.09	0.72	0.178	...	...
Nd: $f_{142+144} =$	0.67	0.32	0.69	0.27	0.510	$0.21^{+0.56}_{-0.21}$	$0.36^{+0.64}_{-0.36}$
Sm: $f_{152+154} =$	0.21	0.64	0.20	0.64	0.495	$0.51 \pm 0.08$	$0.35 \pm 0.14$
Eu: $f_{151} =$	$0.54^{\text{d}}$	0.47	$0.04^{\text{d}}$	0.47	0.478	$0.50 \pm 0.04$	...

<sup>a</sup> Arlandini et al. (1999)

<sup>b</sup> Simmerer et al. (2004); Cowan et al. (2006)

<sup>c</sup> Rosman & Taylor (1998)

<sup>d</sup> The classical fit—based on assuming a smoothly-varying abundance curve—predicts a much smaller *s*-process contribution to  $^{151}\text{Eu}$  than does the stellar *s*-process model of Arlandini et al. (1999). See § 8 for further discussion.

TABLE 3  
HEAVY  $n$ -CAPTURE ELEMENTAL ABUNDANCES IN HD 175305

Species	$Z$	$\log \varepsilon$	$[X/Fe]$	$\sigma$	$N_{\text{lines}}$	$\log \varepsilon_{\odot}$	$\log(gf)$ Ref.	$\log \varepsilon_{\odot}$ Ref.
Ba II	56	+0.91	+0.40	0.16	1	2.13	1	10
La II	57	-0.29	+0.20	0.13	3 <sup>a</sup>	1.13	2	2
Ce II	58	+0.05	+0.09	0.13	3	1.58	3	10
Nd II	60	+0.09	+0.21	0.13	10	1.50	4	10
Sm II	62	-0.25	+0.37	0.11	9	1.00	5	5
Eu II	63	-0.65	+0.46	0.07	3	0.51	6	10
Gd II	64	+0.00	+0.50	0.15	4	1.12	7	10
Dy II	66	+0.01	+0.49	0.16	1	1.14	8	10
Pb I	82	< +0.10	< +0.45	...	1	1.95	9	10

REFERENCES. — (1) Klose et al. (2002); (2) Lawler et al. (2001a); (3) Palmeri et al. (2000); (4) Den Hartog et al. (2003); (5) Lawler et al. (2006); (6) Lawler et al. (2001b); (7) Den Hartog et al. (2006); (8) Wickliffe et al. (2000); (9) Biémont et al. (2000); (10) Grevesse & Sauval (2002)

NOTE. — Ionized species abundance ratios are referenced to the Fe II abundance in Table 3. We adopt the Solar photospheric Fe abundance  $\log \varepsilon_{\odot}(\text{Fe}) = 7.52$  from Sneden et al. (1991).

<sup>a</sup> We synthesize these La II lines using the HFS patterns listed in Table 4 of Ivans et al. (2006).

TABLE 4  
ISOTOPIC HYPERFINE STRUCTURE PATTERNS FOR SAMARIUM

Wavenumber ( $\text{cm}^{-1}$ )	Wavelength ( $\text{\AA}$ )	Component Position ( $\text{cm}^{-1}$ )	Component Position ( $\text{\AA}$ )	Isotope	Strength <sup>a</sup>
22595.910	4424.3373	0.20775	-0.04067	147	0.028106
22595.910	4424.3373	0.13532	-0.02649	147	0.001521
22595.910	4424.3373	0.06911	-0.01353	147	0.000040
22595.910	4424.3373	0.15704	-0.03074	147	0.023908
22595.910	4424.3373	0.09083	-0.01778	147	0.002540
22595.910	4424.3373	0.03117	-0.00610	147	0.000097
⋮	⋮	⋮	⋮	⋮	⋮

NOTE. — The full table is available in machine-readable form in the electronic edition of the journal; only a small portion is shown here to present its general form and content. For lines without full sets of hyperfine A and B constants available (4719, 5052, and 5103), for the  $^{147}\text{Sm}$  and  $^{149}\text{Sm}$  isotopes we list only the isotope shifts, computed as if all A and B values are zero. The isotope shift for the  $^{144}\text{Sm}$  isotope of the 5069 line could not be measured in the FTS spectrum of Lundqvist et al. (2007). We estimate this value by scaling the energy shifts of the  $^{144}\text{Sm}$  isotope relative to the heavier isotopes from the 5052 and 5103 lines, which show similar structure patterns (M. Lundqvist, 2007, private communication).

<sup>a</sup> The sum of the strength values for each line have been normalized to one. When using these components in our spectral synthesis, we divide out the Solar System isotopic ratios as given by Rosman & Taylor (1998), but we stress that this step is NOT included in the data presented here.

TABLE 5  
ISOTOPIC HYPERFINE STRUCTURE PATTERNS FOR NEODYMIUM

Wavenumber ( $\text{cm}^{-1}$ )	Wavelength ( $\text{\AA}$ )	Component Position ( $\text{cm}^{-1}$ )	Component Position ( $\text{\AA}$ )	Isotope	Strength <sup>a</sup>
23932.050	4177.3196	0.10001	-0.01746	143	0.024146
23932.050	4177.3196	0.14184	-0.02476	143	0.001719
23932.050	4177.3196	0.05369	-0.00937	143	0.019886
23932.050	4177.3196	0.17828	-0.03112	143	0.000061
23932.050	4177.3196	0.09013	-0.01573	143	0.002841
23932.050	4177.3196	0.01208	-0.00211	143	0.016161
⋮	⋮	⋮	⋮	⋮	⋮

NOTE. — The full table is available in machine-readable form in the electronic edition of the journal; only a small portion is shown here to present its general form and content.

<sup>a</sup> The sum of the strength values for each line have been normalized to one. When using these components in our spectral synthesis, we divide out the Solar System isotopic ratios as given by Rosman & Taylor (1998), but we stress that this step is NOT included in the data presented here.

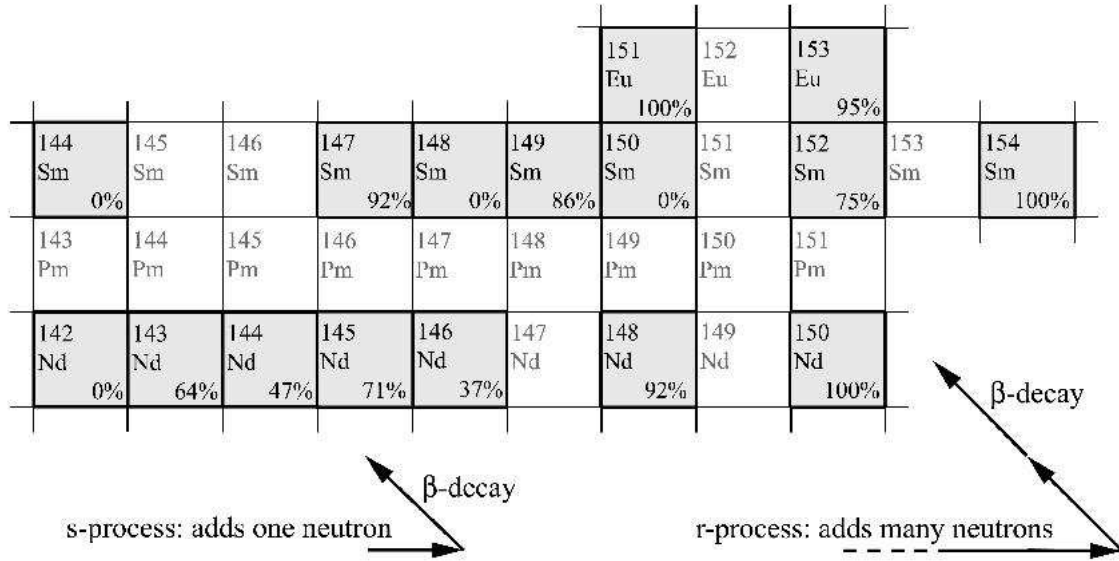


FIG. 1.— A small region of the table of nuclides, showing increasing mass number ( $A$ ) on the horizontal axis and increasing atomic number ( $Z$ ) on the vertical axis. Naturally-occurring isotopes are represented by the gray squares. The figure highlights the naturally-occurring isotopes of neodymium (Nd,  $Z = 60$ ), samarium (Sm,  $Z = 62$ ), and europium (Eu,  $Z = 63$ ); promethium (Pm,  $Z = 61$ ) has no naturally-occurring isotopes. We also show the predicted percentage of  $r$ -process material in the S. S. abundance for each isotope as given by Cowan et al. (2006). This figure illustrates the pathways by which the  $s$ - and  $r$ -processes operate and the resulting differences in the  $s$  or  $r$  fraction of S. S. material.

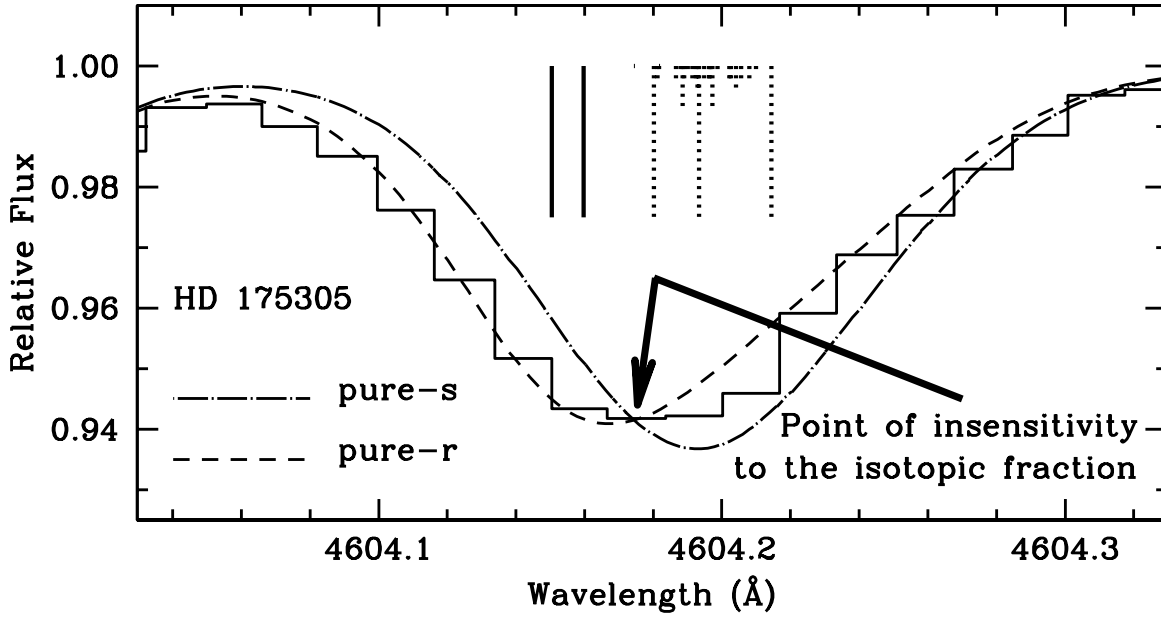


FIG. 2.— One method used to match the observed and synthetic spectra, displaying how the point of insensitivity has been matched to the observed spectrum. The pure-*s*- and pure-*r*-syntheses are indicated by dot-dashed and dashed lines, respectively. The observed spectrum is represented by the histogram. The point at which the pure-*s*- and pure-*r*-process syntheses intersect is defined to be the point of insensitivity to the isotopic mix. We adjust the wavelength of the synthetic spectra so that the point of insensitivity coincides with the center of the nearest pixel in the observed spectrum. The isotopic fraction can then be measured using the fitting algorithm. The vertical sticks represent the positions and relative strengths of the individual hyperfine components; solid sticks represent the  $^{152}\text{Sm}$  and  $^{154}\text{Sm}$  isotopes, while dashed sticks represent the remaining five isotopes.

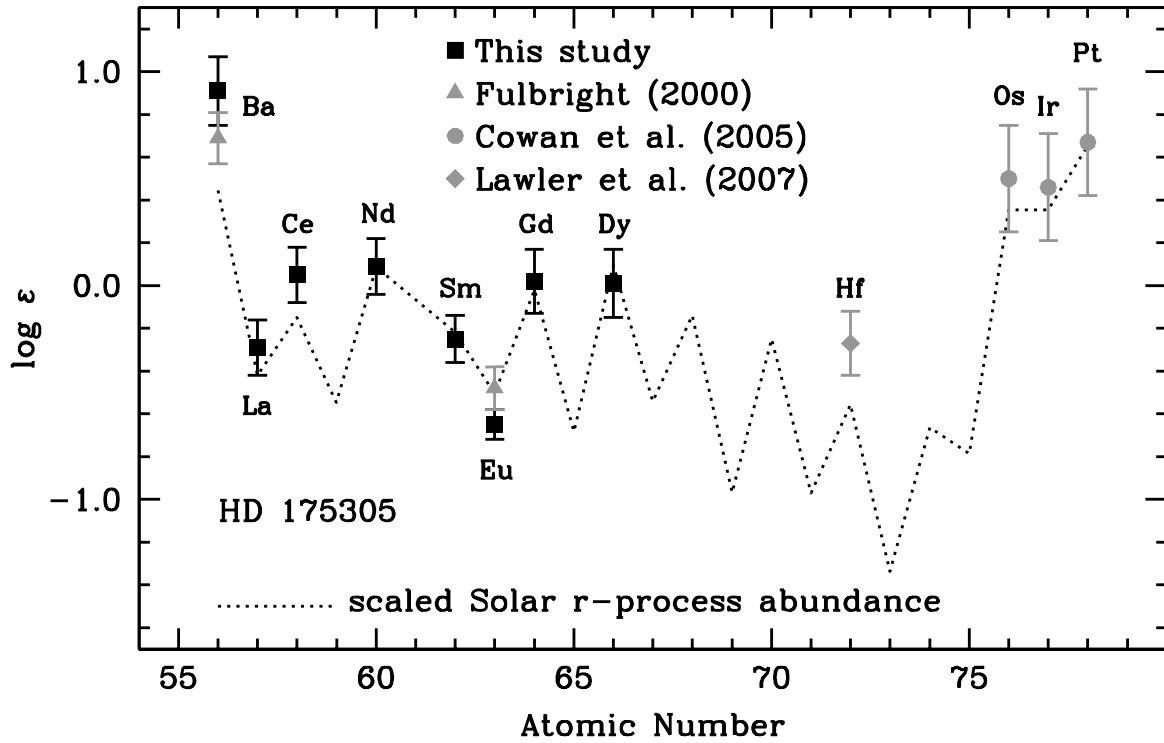


FIG. 3.— Heavy  $n$ -capture elemental abundances for HD 175305. Black squares indicate our observed abundances. Gray triangles indicate the observed Ba and Eu abundances from Fulbright (2000). Gray circles indicate the observed Os, Ir, and Pt abundances from Cowan et al. (2005). The gray diamond indicates the observed Hf abundance from Lawler et al. (2007). The dotted line shows the scaled S. S.  $r$ -process abundances of Simmerer et al. (2004), normalized to Fulbright (2000)'s Eu abundance. The figure suggests that the scaled Solar  $r$ -process abundances provide a respectable fit to the observed abundances beyond Ba.

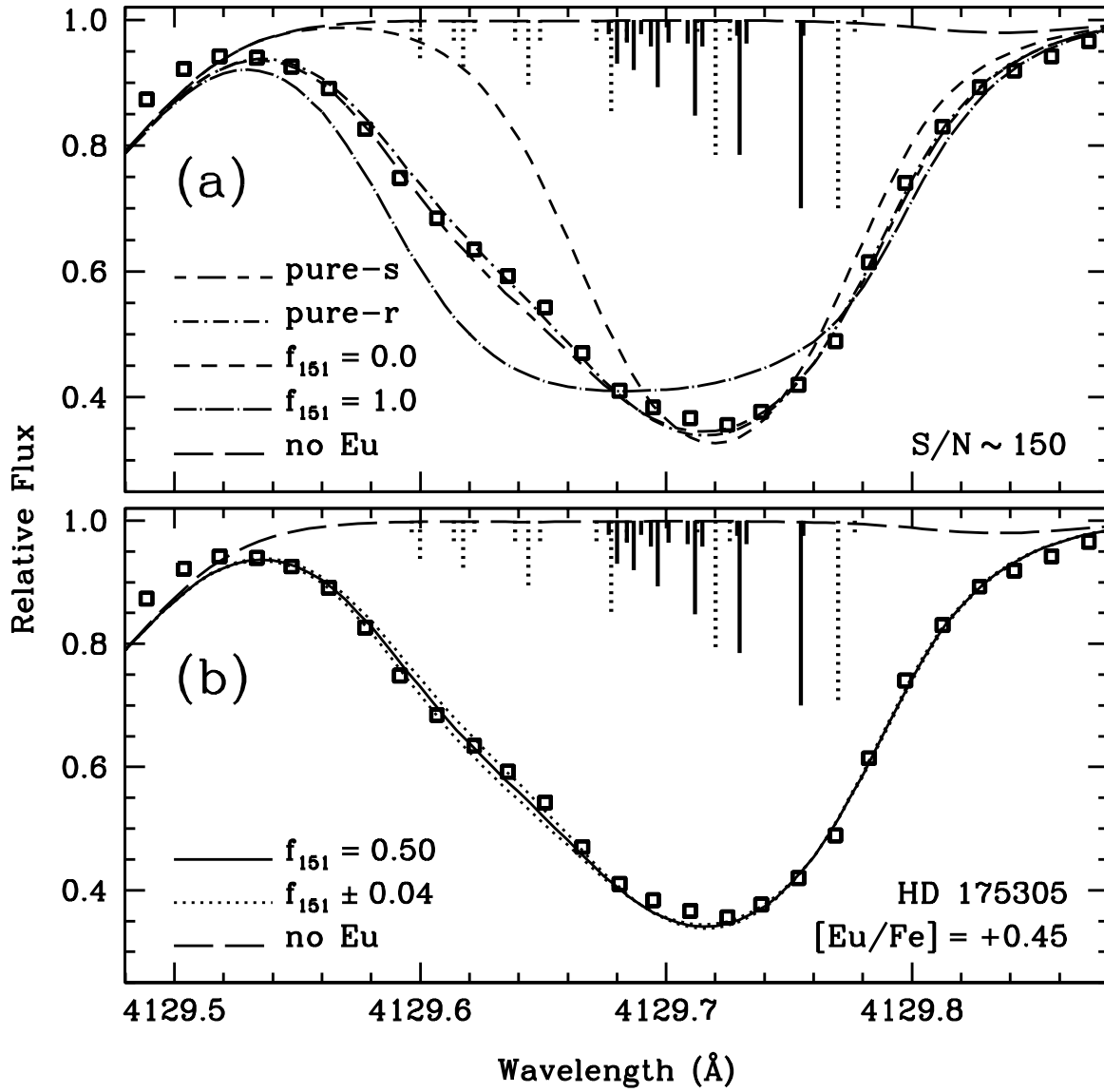


FIG. 4.— Our synthesis of the Eu II line at 4129Å in HD 175305. We have measured an isotopic fraction of  $f_{151} = 0.50 \pm 0.04$  for this line. The observed spectrum is indicated by open squares. In panel a, we show the syntheses with the extreme values of  $f_{151}$  as well as the pure-*s*- and pure-*r*-process syntheses. In panel b, the solid curve represents our best fit isotopic fraction, while the dotted curves represent the  $3\sigma$  uncertainties. In both panels, the long-dashed curve is a synthesis with no Eu present, indicating that this line is generally free of blending features. The vertical sticks represent the positions and relative strengths of the individual hyperfine components; dotted sticks represent  $^{151}\text{Eu}$  while solid sticks represent  $^{153}\text{Eu}$ . Note that the Eu elemental abundance reported is the best-fit value for this synthesis and not our derived Eu abundance for HD 175305.

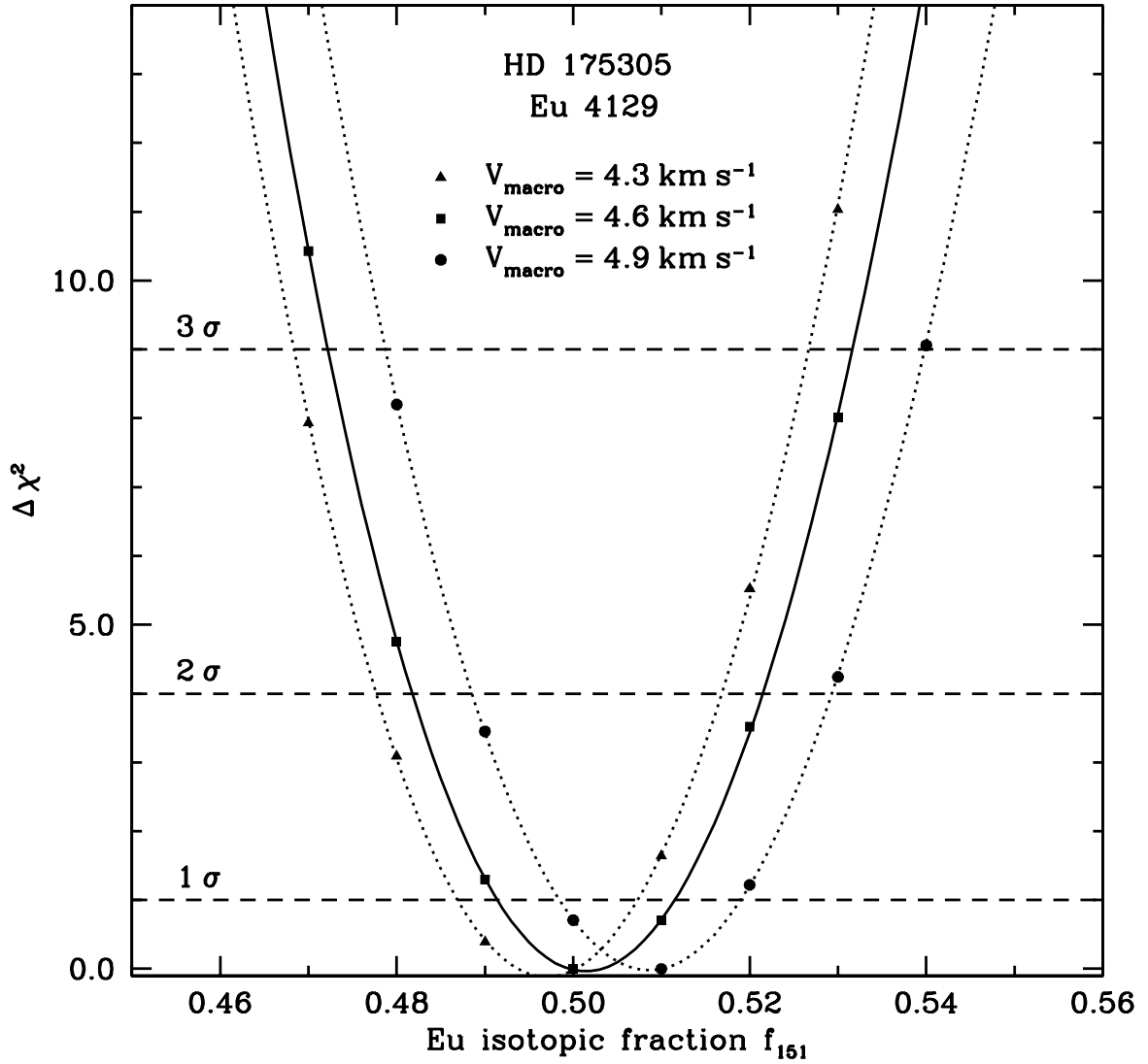


FIG. 5.—  $\Delta\chi^2$  values for the Eu 4129 line in HD 175305, shown for three values of  $V_{\text{macro}}$ . The solid line is a third-order polynomial fit to the measured  $\Delta\chi^2$  values for the best value of  $V_{\text{macro}}$ ,  $4.6 \text{ km s}^{-1}$ , and the dotted lines are fits to the measured  $\Delta\chi^2$  values for the uncertainties in  $V_{\text{macro}}$ . One, two, and three- $\sigma$  confidence intervals are indicated by the dashed lines. The fits have well-defined minima, and the choice of the macro-turbulent velocity has little effect on the derived isotopic fraction.

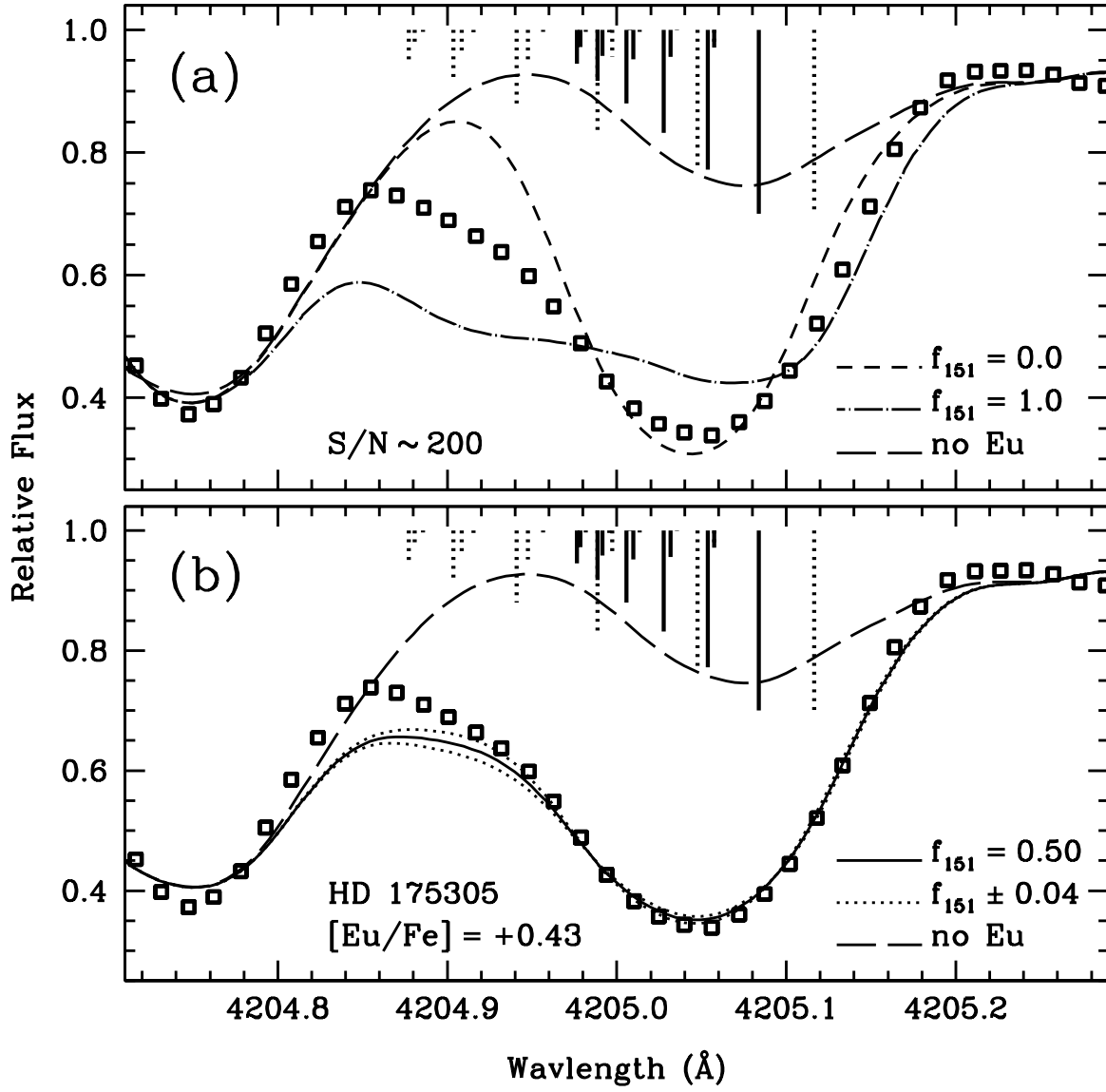


FIG. 6.— Our synthesis of the Eu II line at 4205 Å in HD 175305. Symbols are the same as in Figure 4. We emphasize that the isotopic fraction shown in panel **b** is the value derived from the 4129 Å line and not a fit to this line. Note the strong blends. The isotope fraction derived from the 4129 Å line provides a reasonable fit to the 4205 Å line as well, requiring only small changes in the elemental abundance.

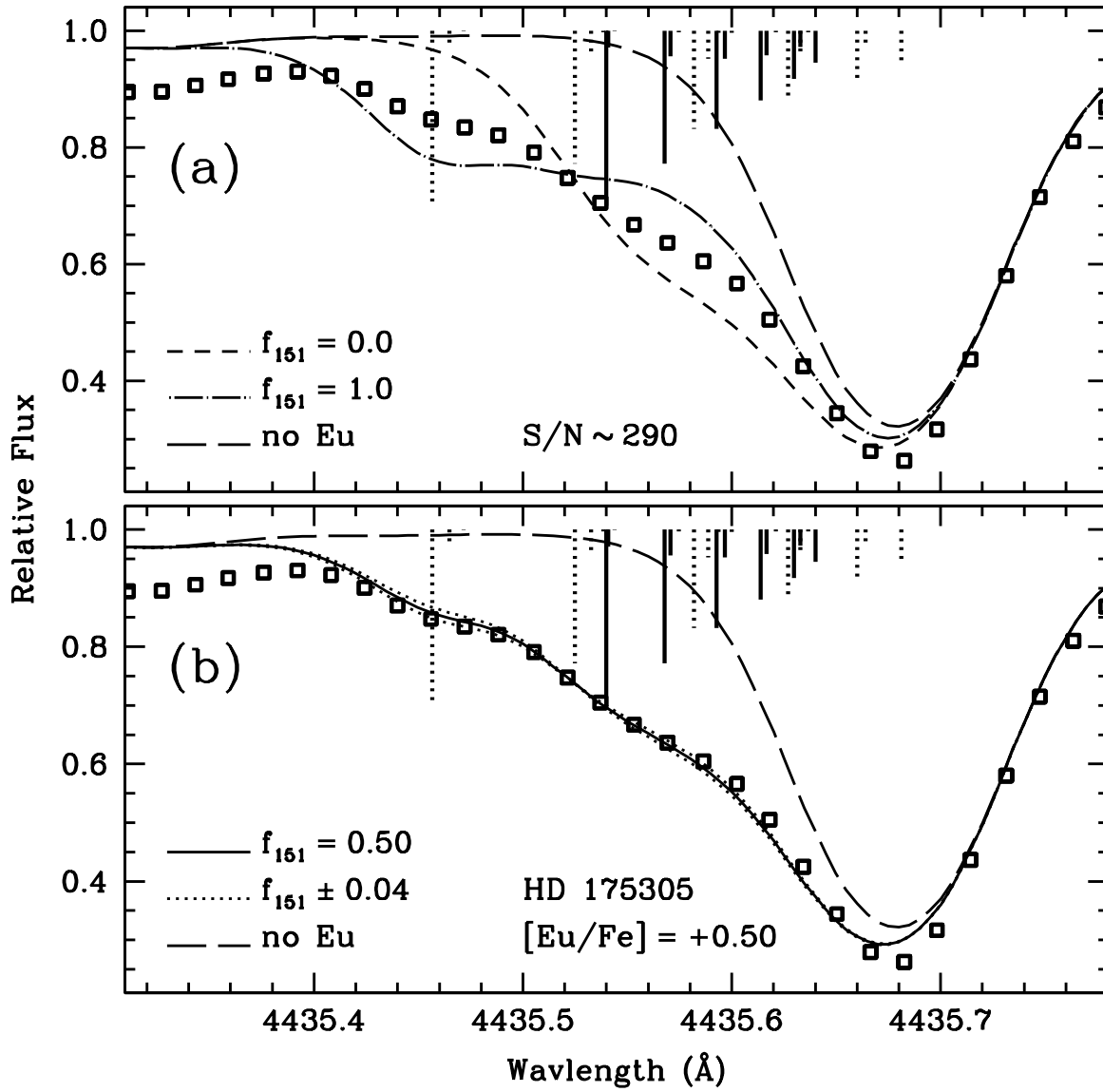


FIG. 7.— Our synthesis of the Eu II line at 4435 Å in HD 175305. Symbols are the same as in Figure 4. We emphasize that the isotopic fraction shown in panel **b** is the value derived from the 4129 Å line and not a fit to this line. Note the strong blend with the saturated Ca I line at 4535.67 Å. The isotope fraction derived from the 4129 Å line provides a reasonable fit to the 4435 Å line as well, requiring only small changes in the elemental abundance.

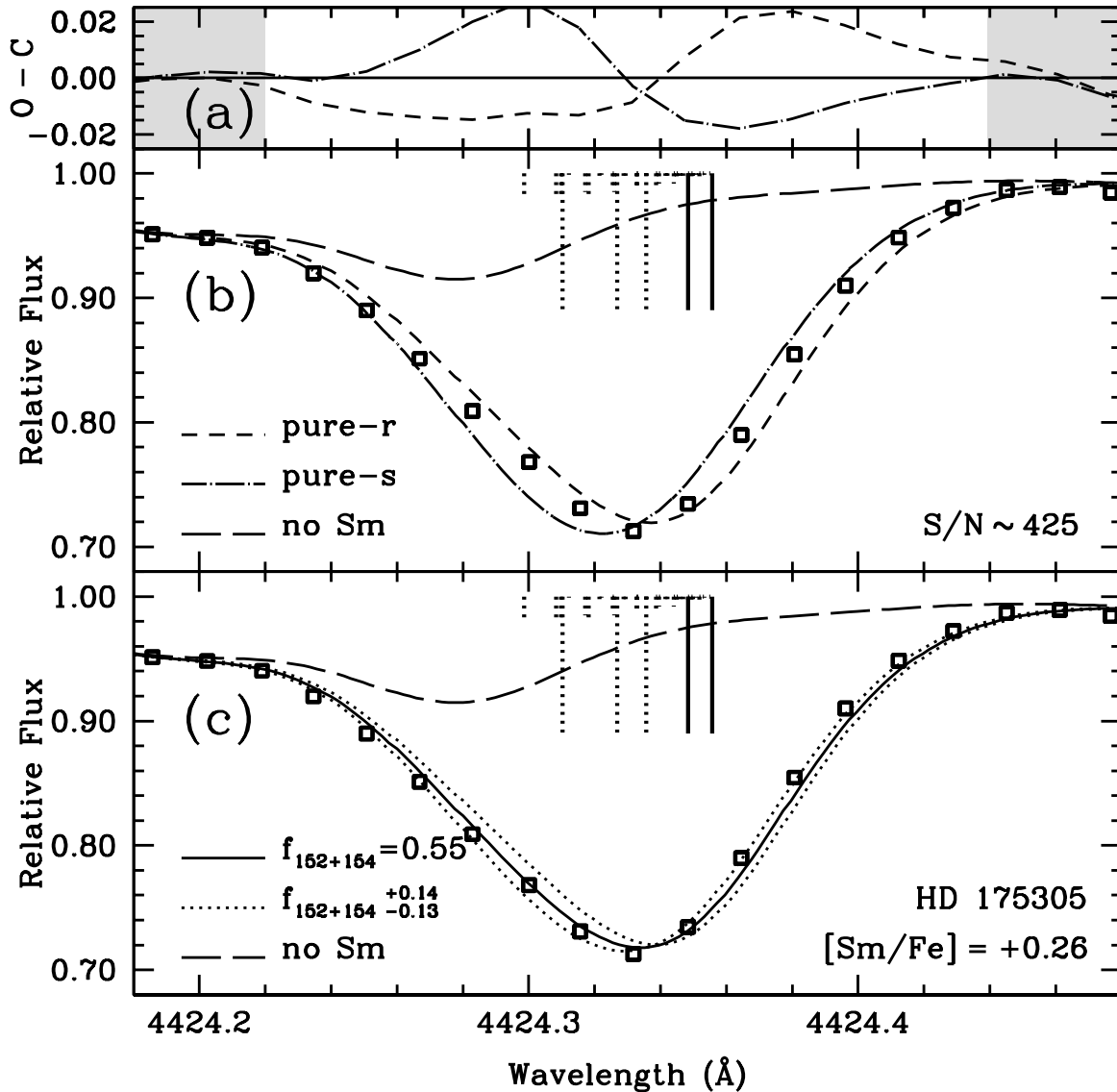


FIG. 8.— Our synthesis of the Sm II line at 4424Å in HD 175305. The observed spectrum is indicated by open squares. In panel a, we show an  $(O - C)$  plot for the pure- $s$ - and pure- $r$ -process syntheses shown in panel b. The unshaded region indicates the wavelengths over which we measure the isotopic fraction using the  $\chi^2$  algorithm. In panel b, we show syntheses for the pure- $s$ - and pure- $r$ -process syntheses (the dot-dashed and short-dashed curves, respectively) illustrating the contrast between these extremes. In panel c, we show the synthesis of our best fit, represented by the solid curve, and the  $3\sigma$  uncertainties, represented by the dotted curves. The long-dashed curve is a synthesis with no Sm present, indicating the presence of blending features. The vertical sticks represent the positions and relative strengths of the individual hyperfine components; solid sticks represent the two heaviest isotopes, while dashed sticks represent the lighter five isotopes. We measure a Sm isotopic fraction of  $f_{152+154} = 0.55^{+0.14}_{-0.13}$  for this line, which suggests an  $r$ -process origin. Note that the Sm elemental abundance reported is the best-fit value for this line only and not our mean  $[Sm/Fe]$  in HD 175305.

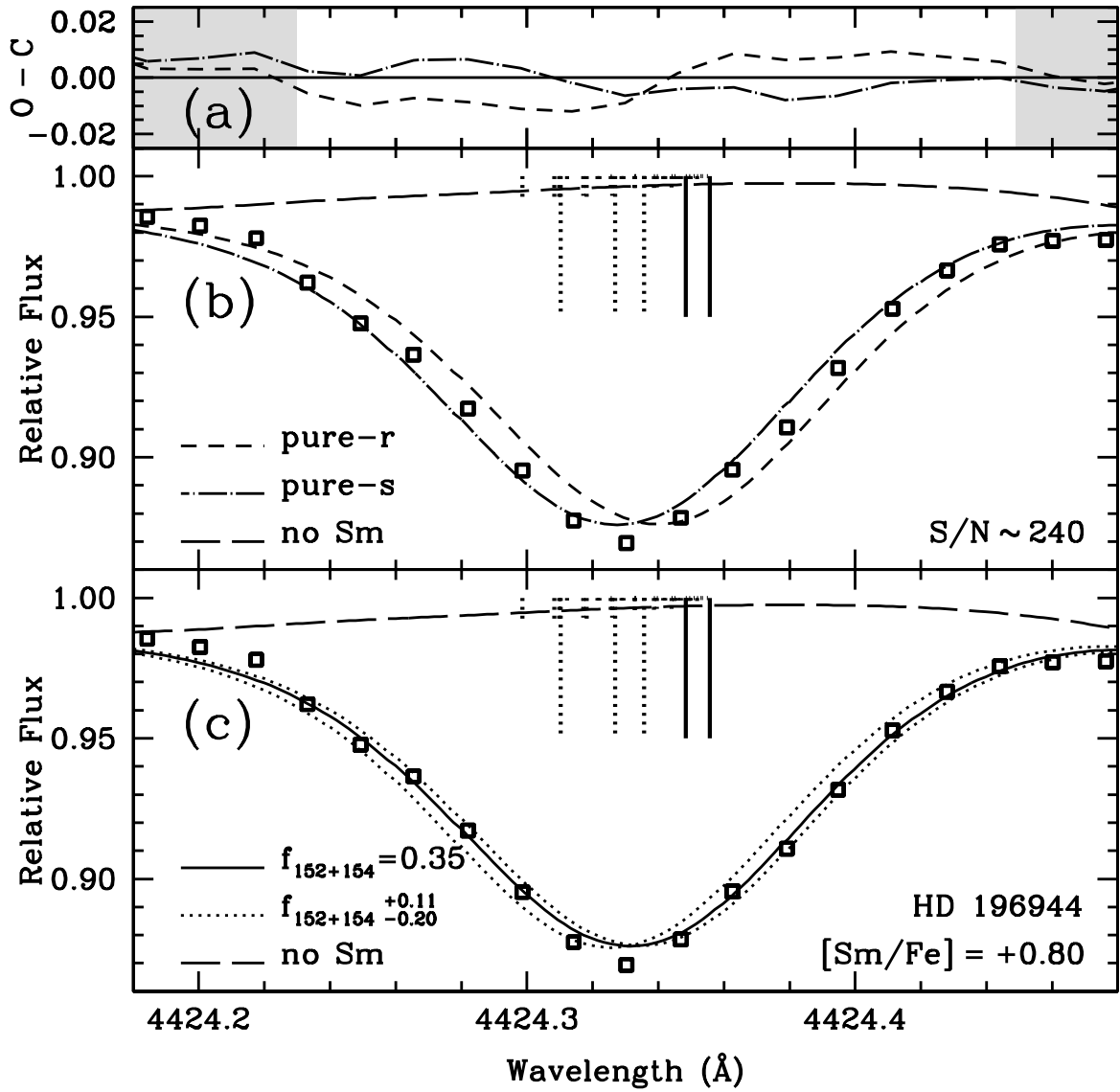


FIG. 9.— Our synthesis of the Sm II line at 4424Å in HD 196944. Symbols are the same as in Figure 8. We measure a Sm isotopic fraction of  $f_{152+154} = 0.35^{+0.11}_{-0.20}$  for this line, which moderately suggests an *s*-process origin. Note that the Sm elemental abundance reported is the best-fit value for this line only and not our mean  $[\text{Sm}/\text{Fe}]$  in HD 175305.

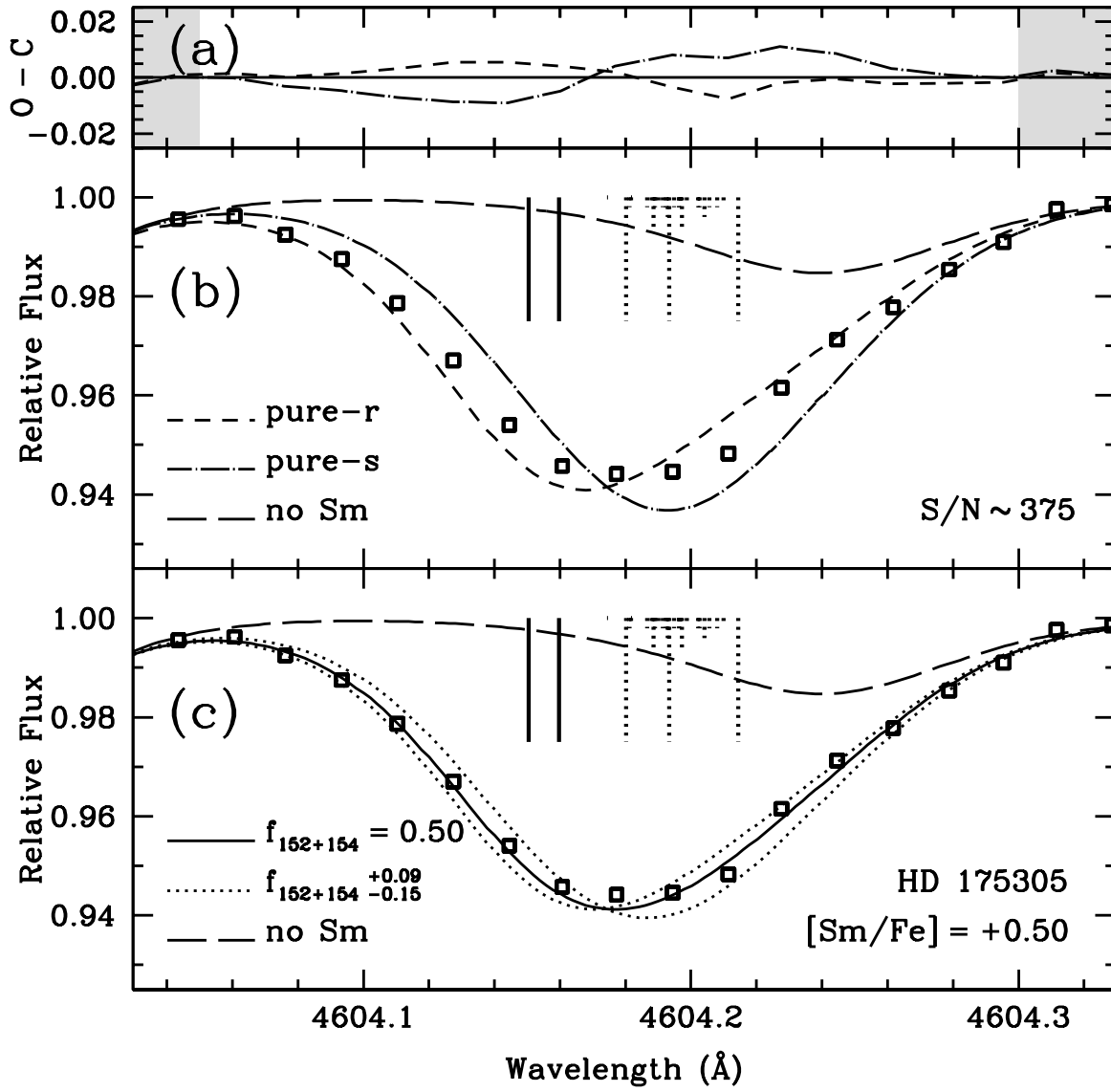


FIG. 10.— Our synthesis of the Sm II line at 4604Å in HD 175305. Symbols are the same as in Figure 8. We measure a Sm isotopic fraction of  $f_{152+154} = 0.50^{+0.09}_{-0.15}$  from this line, which suggests an  $r$ -process origin. Note that the Sm elemental abundance reported is the best-fit value for this line only and not our mean [Sm/Fe] in HD 175305.

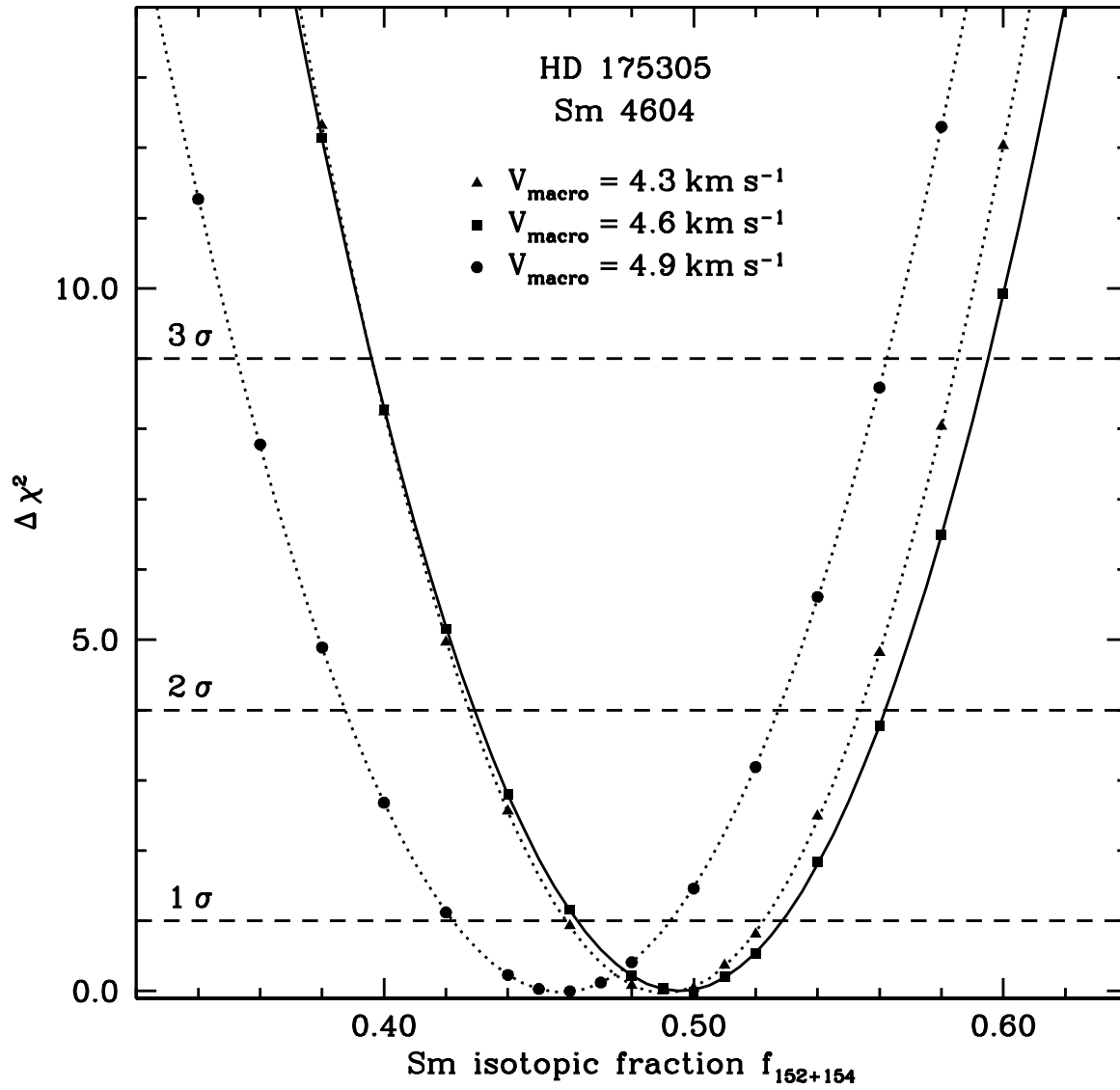


FIG. 11.—  $\Delta\chi^2$  values for the Sm 4604 line in HD 175305, shown for three values of  $V_{\text{macro}}$ . Symbols are the same as in Figure 5. Here the macroturbulence has only a small effect on the derived isotopic fraction. Similar results are found for the Sm 4424 line in both HD 175305 and HD 196944.

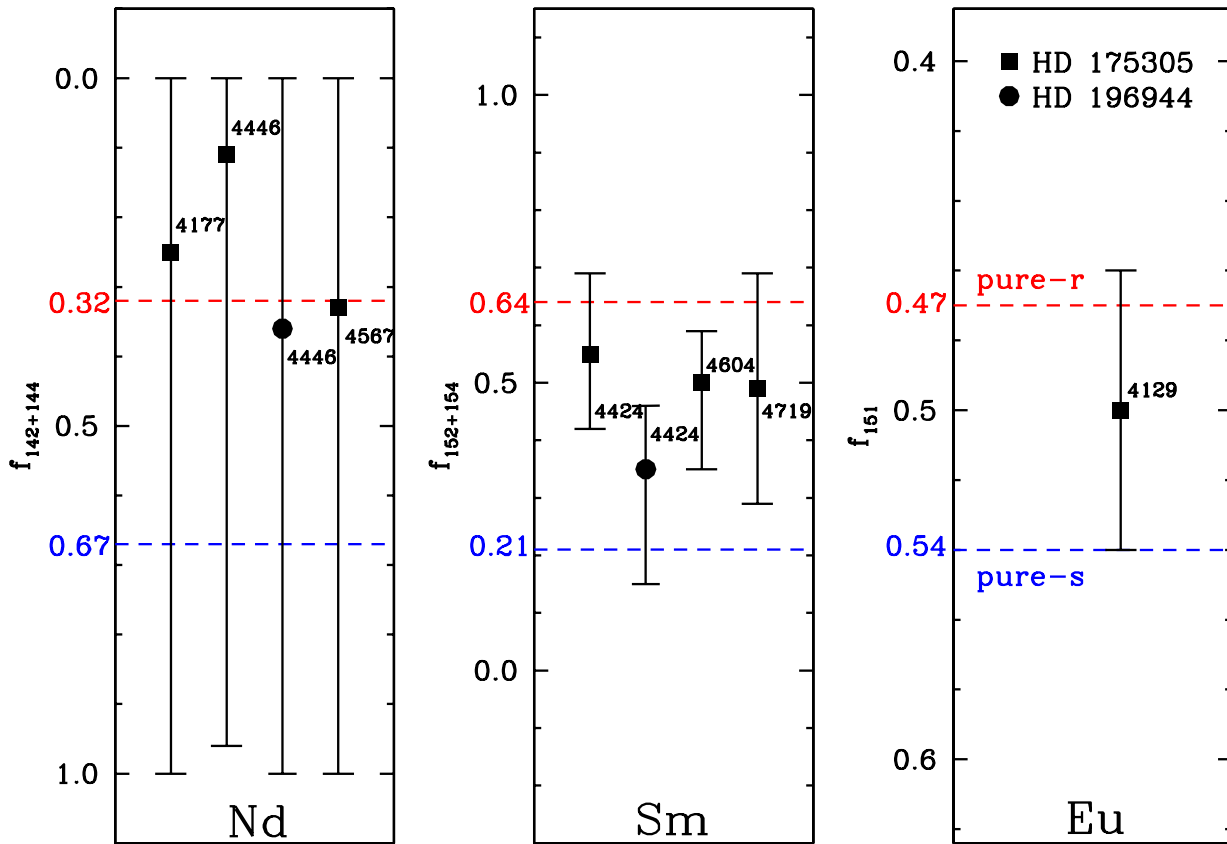


FIG. 12.— A summary of our best isotopic fraction measurements for each species. The Nd isotopic fractions reported here were measured by the method of matching the observed and synthetic spectra at the point of insensitivity to the isotopic mix. The Sm and Eu isotopic fractions were measured by fitting the shape of the line profile. Squares represent measurements in HD 175305, while circles represent measurements in HD 196944. The dotted line and dashed line (colored blue and red, respectively, in the electronic edition) represent the pure-*s*- and pure-*r*-process predictions of Arlandini et al. (1999). The differences between the pure-*s*- and pure-*r*-process predictions are scaled together to emphasize the relative precision with which the two processes can be distinguished by each species. [See electronic edition for a color version of this figure.]

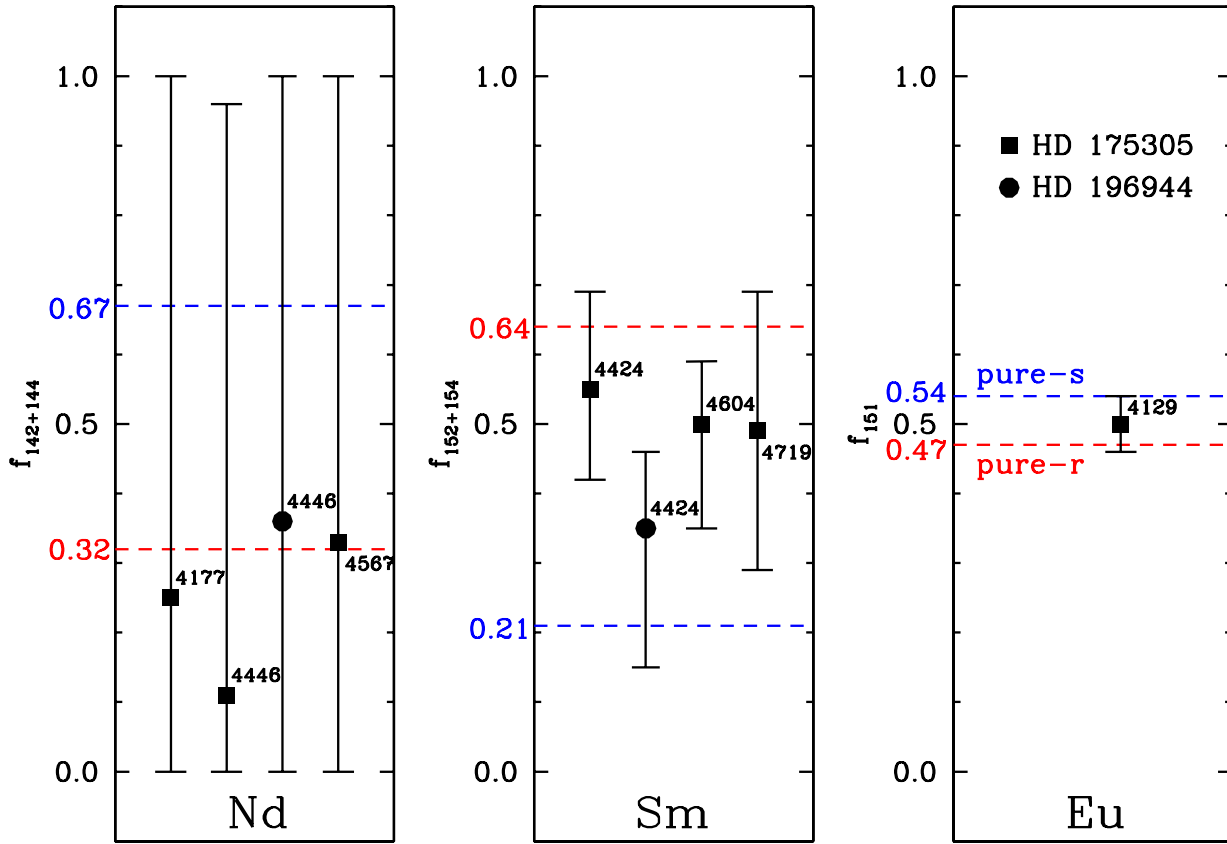


FIG. 13.— A summary of our best isotopic fraction measurements for each species. The data and symbols are the same as in Figure 12. The measurements are cast here in an absolute sense, emphasizing the relative precision with which each species was measured. [See electronic edition for a color version of this figure.]

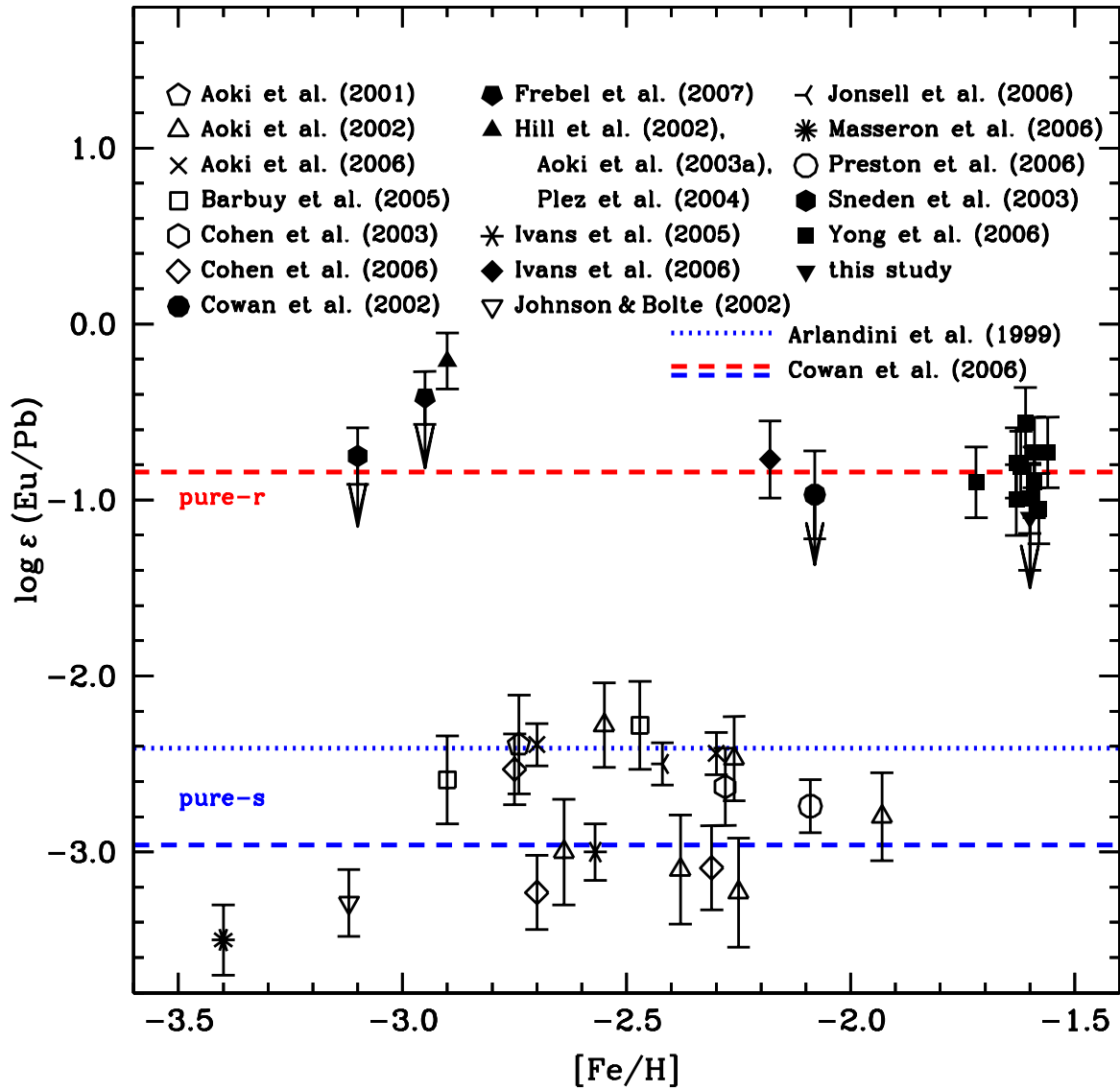


FIG. 14.— The  $\log \epsilon$  (Eu/Pb) abundance as a function of [Fe/H] for 36 halo and globular cluster stars collected from the literature or measured in our study. References for the individual stars are indicated in the figure. Solid shapes indicate stars classified as  $r$ -process enriched, open shapes indicate stars classified as  $s$ -process enriched, and starred shapes indicate stars classified as  $(r+s)$ -process enriched. Upper limits are indicated with downward arrows. The abundance predictions from Arlandini et al. (1999) and Cowan et al. (2006) are shown as dotted and dashed lines, respectively. (In the electronic edition, blue and red lines represent the pure- $s$ -process and pure- $r$ -process abundance predictions.) The  $s$ - and  $(r+s)$ -process-enriched stars cannot unambiguously distinguish between the different pure- $s$  abundance predictions. [See electronic edition for a color version of this figure.]

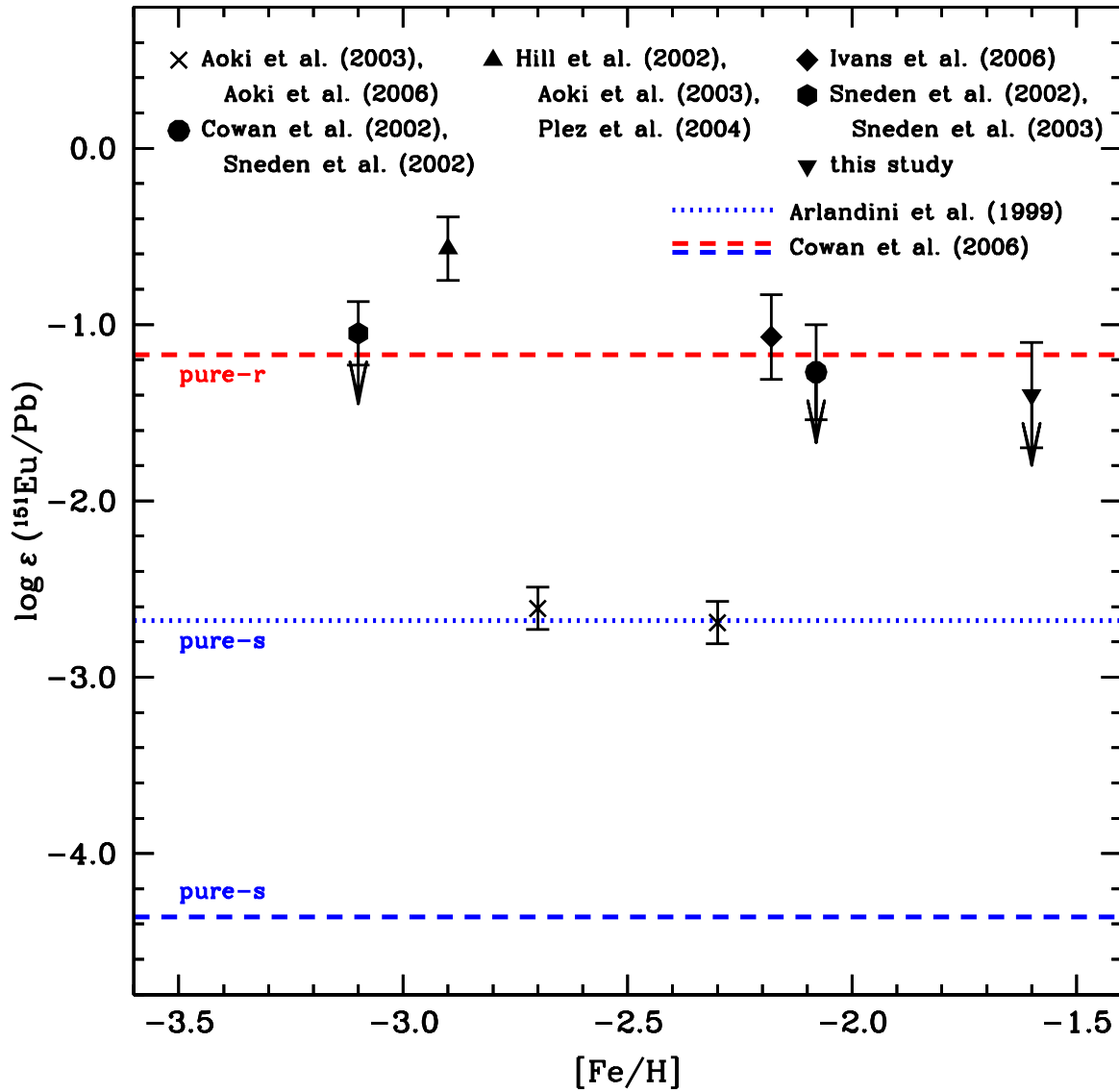


FIG. 15.— The  $\log \varepsilon(^{151}\text{Eu}/\text{Pb})$  abundance as a function of  $[\text{Fe}/\text{H}]$  for 7 halo stars collected from the literature or measured in our study. References for the individual stars are indicated in the figure. Symbols are the same as in Figure 14. The two  $(r+s)$ -enriched stars favor the pure- $s$   $^{151}\text{Eu}$  abundance prediction of Arlandini et al. (1999). [See electronic edition for a color version of this figure.]

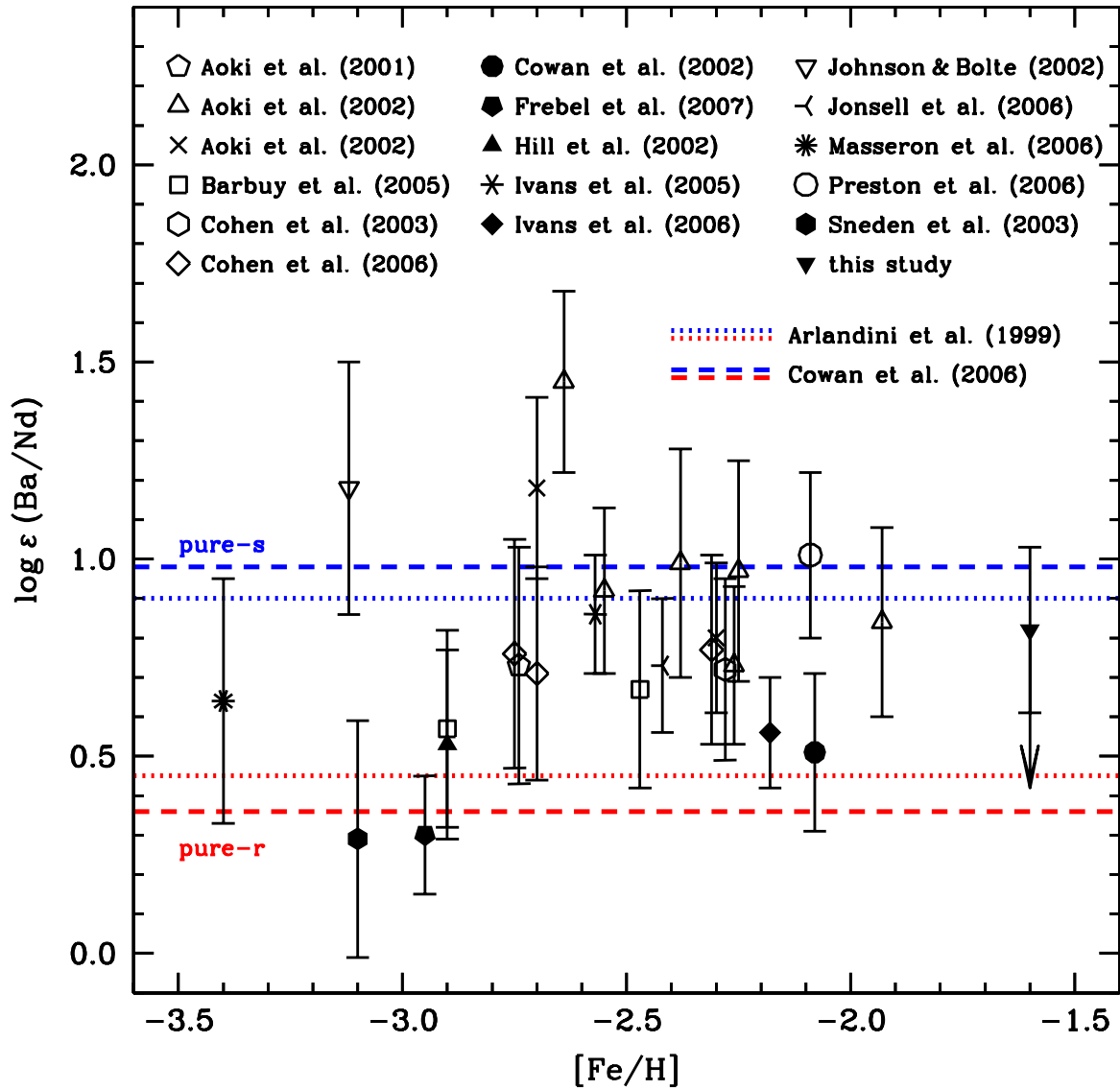


FIG. 16.— The  $\log \epsilon$  (Ba/Nd) abundance as a function of [Fe/H] for 26 halo stars collected from the literature or measured in our study. References for the individual stars are indicated in the figure. Symbols are the same as in Figure 14. No distinction is observed between the  $s$ - and  $(r+s)$ -enriched stars from their Ba and Nd abundances, leading us to conclude that the two  $(r+s)$ -enriched stars in Figure 15 are representative of stars containing products of predominantly- $s$ -process-enriched material. [See electronic edition for a color version of this figure.]